P-wave tomography beneath Greenland and surrounding regions–I. Crust and upper mantle

Genti Toyokuni[1*], Takaya Matsuno[1], and Dapeng Zhao[1]

[1] Department of Geophysics, Graduate School of Science, Tohoku University, Sendai 980-8578, Japan

Submitted to ***Journal of Geophysical Research: Solid Earth*** in March 2020

*Corresponding author:

Genti Toyokuni

E-mail: toyokuni@tohoku.ac.jp

ORCID ID: 0000-0003-3786-207X

Key Points:

- 3-D P-wave velocity structure of the crust and upper mantle beneath Greenland and surrounding regions is investigated.
- A remarkable low-velocity anomaly elongated in the NW-SE direction is revealed at depths shallower than 250 km beneath central Greenland.
- The anomaly may reflect the residual heat when the Greenlandic plate passed over the Iceland and Jan Mayen plumes.

Abstract

We study the 3-D P-wave velocity (Vp) structure of the crust and upper mantle beneath Greenland and surrounding regions using the latest P-wave arrival-time data. The Greenland Ice Sheet Monitoring Network (GLISN), initiated in 2009, is an international project for seismic observation in these regions, and currently operating 35 seismic stations. We use a regional-scale seismic tomography method to simultaneously invert both absolute P-wave arrival times of local earthquakes and P-wave relative travel-time residuals of teleseismic events. These data are extracted from the ISC-EHB catalog, but for the teleseismic events, we newly picked arrival times from seismograms using the cross-correlation analysis. In the tomographic inversion, the grid intervals in the longitudinal direction depend on the latitude in the polar regions, so we apply the coordinate transformation that moves the study region to the equator. Our results reveal a remarkable low-Vp anomaly elongated in the NW-SE direction at depths ≤ 250 km beneath central Greenland, which may reflect the residual heat when the Greenlandic plate passed over the Iceland plume at ~80−20 Ma. Although previous studies have suggested this feature, our results first show that the low-Vp zone is within the Greenlandic lithosphere and its spatial distribution agrees very well with the high crustal heat-flow regions. Our results also indicate possible existence of residual heat from the Jan Mayen plume.

Plain Language Summary

Greenland is a stable land mass and has preserved ~4 billion years of Earth's history. In the vicinity of the island, there are the Mid-Atlantic Ridge, the Iceland and Jan Mayen hotspot volcanos, and a geothermal area of western Svalbard, which indicate importance of these regions for understanding the global-scale tectonics and history of the Earth. Seismic tomography is a well-established method to obtain 3-D images of underground structure by inverting observed arrival times of seismic waves for a huge number of source-station pairs. In this work we apply seismic tomography to analyze the latest data recorded by a new seismograph network, and we obtain detailed 3-D images of the crust and upper mantle beneath Greenland and surrounding regions. We find a low seismic velocity zone running in the NW-SE direction beneath central Greenland. This zone is located within the Greenlandic plate, and its spatial distribution agrees very well with an area with a high crustal heat-flow. These new results suggest that the low-velocity zone reflects the residual heat from the Iceland plume transmitted when the Greenlandic plate passed over the plume at ~80−20 Ma. We also find a possible heat track left by the Jan Mayen plume.

1 Introduction

Greenland, located in the Arctic region, is the largest island in the world. The land area extends 2,675 km in N-S and 1,250 km in E-W [*Henriksen et al.*, 2009], spanning over 20° in the central angle of the Earth. However, at present, we know only a small part of the island because 80% of the land area is covered by thick ice called Greenland Ice Sheet (GrIS). Geological studies of the exposure regions show that most of the crust is cratonic, which records the Earth's history of ~4 billion years since the Archean times. Therefore, the seismicity in Greenland is very low, and there is no active volcano; distribution of hot springs only shows geothermal activity in this island [*Hjartarson and Armannsson*, 2010]. On the other hand, the Mid-Atlantic Ridge is located just east of Greenland, where the North American plate on the Greenland side and the Eurasian plate on the opposite side exist and the seismicity is very active. Along the ridge, there are the Iceland and Jan Mayen volcanoes known as hot spots and a geothermal area of western Svalbard [*Dumke et al.*, 2016], showing tectonic activity and attraction of these regions (Figure 1).

Before 2008, there were only a few permanent seismic stations in Greenland, including only one station on the GrIS (station code: SUMG). Recent global climate change has been causing enhancement of cryoseismic activities mainly at the terminus of glaciers [e.g., *Ekström et al.*, 2003, 2006], which resulted in widespread attention to seismic monitoring of the GrIS. Under such circumstances, in 2009, an international project "Greenland Ice Sheet monitoring Network (GLISN)" was launched [*Clinton et al.*, 2014; *Toyokuni et al.*, 2014]. It is a project to deploy a broadband seismic observation network in Greenland and surrounding regions, and currently the following eleven countries are collaborating: Canada, Denmark, France, Germany, Italy, Japan, Norway, Poland, South Korea, Switzerland, and the USA. The practical purposes of

the GLISN project are to install and maintain new seismic and GPS stations, and to integrate the existing permanent seismic stations that had been independently operated by each country. Currently, 35 GLISN stations are in operation (Table S1, Figure 2). In particular, a joint USA and Japanese team has been maintaining three new stations on the GrIS (DY2G, ICESG, and NEEM), which largely homogenized the spatial distribution of the GLISN stations. In 2014, the world's first real-time transmission of broadband, three-component, and continuous seismic waveform data from the ice sheet was successfully completed, and now high-quality seismic waveforms can be downloaded immediately worldwide through the Data Management Center (DMC), a branch of the Incorporated Research Institutions for Seismology (IRIS), USA. Seismological analyses of Greenland and surrounding regions were scarce before the GLISN network was established [*Dahl-Jensen et al.*, 2003b; *Darbyshire et al.*, 2004; *Pilidou et al.*, 2004; *Braun et al.*, 2007; *Jakovlev et al.*, 2012], but recently they have been actively conducted using the GLISN data [e.g., *Rickers et al.*, 2013; *Mordret et al.*, 2016; *Levedev et al.*, 2017; *Levshin et al.*, 2017; *Darbyshire et al.*, 2018; *Pourpoint et al.*, 2018; *Toyokuni et al.*, 2018].

Seismic tomography is a powerful tool to obtain detailed 3-D images of underground structure. The crust and upper mantle structure beneath Greenland has been investigated by using several tomographic methods with various spatial scales, including regional-scale surface wave tomography [*Darbyshire et al.*, 2004; *Levshin et al.*, 2017; *Darbyshire et al.*, 2018; *Pourpoint et al.*, 2018], body wave tomography in the whole Arctic region [*Jakovlev et al.*, 2012], full wave tomography in the North Atlantic region [*Rickers et al.*, 2013], and full wave tomography in the whole Arctic region [*Levedev et al.*, 2017]. Many of these previous studies discussed the relationship between a low-velocity (low-V) anomaly elongated in the E-W direction beneath central Greenland and the ancient track of the Iceland plume that was estimated to form at

~80−20 Ma [e.g., *Matthews et al.*, 2016]. However, these tomographic results showed large discrepancies, and the low-V anomaly was not clearly imaged near the surface. For example, *Jakovlev et al.* [2012], *Pourpoint et al.* [2018], *Rickers et al.* [2013], and *Levedev et al.* [2017] reported the low-V anomaly only within a depth range of 100–200 km, whereas *Darbyshire et al.* [2018] did not find such an anomalous zone. Underground temperature conditions should also be closely related to thermal activity at the surface. There are many hot springs in eastern Greenland [*Hjartarson and Armannsson*, 2010]. In addition, previous studies examining the crustal heat flow have found a high heat-flow region running NW-SE through central Greenland [e.g., *Rogozhina et al.*, 2016; *Martos et al.*, 2018; *Artemieva*, 2019], which is also considered as the heat track due to the Iceland plume. However, no previous study discussed the relationship between these observations and seismic velocity structures.

To date, no detailed body-wave tomography has been performed for Greenland and surrounding regions. The purpose of this study is to obtain a detailed 3-D P-wave velocity model from the surface to the upper mantle beneath these regions by analyzing the data recorded by the latest seismic observation network (GLISN), and to improve our knowledge on the underground structures and tectonics in the study region (Figure 1).

2 Methods and Data

2.1 Regional tomography

Considering the lateral extent of Greenland and the depth range of our interest, we adopt the regional tomography approach, which treat areas with horizontal distances of ~1000 km [*Zhao*, 2015]. Regional tomography usually uses both local and teleseismic data [e.g., *Zhao et*

130 *al.*, 1994, 2012]. Seismic rays from the local events can be traced completely within the study
131 region, so we can use absolute travel-time residuals

132

$$t_{ij} = T_{ij}^{\mathrm{OBS}} - T_{ij}^{\mathrm{CAL}}, \tag{1}$$

133

134 for tomographic inversion, where T_{ij}^{OBS} and T_{ij}^{CAL} are, respectively, observed and calculated
135 (theoretical) arrival times from ith event to jth station. On the other hand, for the teleseismic
136 events with large epicentral distances (~30°−100°), we only consider portions of the seismic rays
137 that are located in the study volume. The effect of structural heterogeneity outside the study
138 volume is reduced by assuming that, for each event, the effect is common to travel-time residuals
139 at all seismic stations in the study region. Therefore, in the tomographic inversion we use the
140 relative travel-time residuals of teleseismic events:

141

$$\begin{aligned} r_{ij} &= t_{ij} - \overline{t_i}, \\ \overline{t_i} &= \frac{1}{n_i}\sum_{j=1}^{n_i} t_{ij}, \end{aligned} \tag{2}$$

142

143 where $\overline{t_i}$ is the average of absolute travel-time residuals at all stations representing the influences
144 of structural heterogeneity outside the study volume and the errors in hypocentral parameters,
145 and n_i is the number of recording stations of the ith event.

146 We apply the seismic tomography method of *Zhao et al.* [1994, 2012] to analyze our data
147 set. This method discretizes the structure on 3-D grid nodes arranged in the study volume, and
148 can treat complex-shaped velocity discontinuities (e.g., the Moho) in the study region.
149 Theoretical arrival times are calculated through 3-D ray tracing by combining the pseudo-

bending scheme [*Um and Thurber*, 1987] and Snell's law [*Zhao et al.*, 1992]. The tomographic inversion is conducted using the LSQR algorithm [*Paige and Saunders*, 1982] with damping and smoothing regularizations [*Zhao et al.*, 1992, 2012].

2.2 Coordinate transformation

In the polar regions, the meridians become denser at higher latitudes, so when grid nodes are arranged at equal angular intervals in latitude and longitude, the grid distribution is strongly biased. The bias causes the following problems: (1) as the grid spacing becomes narrower, the ray density per grid node is reduced, so the solution at that grid node becomes unstable, and (2) when the smoothing procedure is applied to the tomographic inversion, it sometimes uses the values on a particular node and its adjacent nodes. Thus, if the adjacent nodes are very close, the smoothing is only effective to spatially very narrow areas and thus the resulting tomographic patterns are localized. When the calculation is conducted in the high latitude regions, the problem (2) localizes the pattern along the meridian.

In order to solve these problems, a flexible grid method that arranges grid nodes at irregular intervals [*Zhao*, 2009], and a method that moves the study region to the equator by global coordinate transformation [*Kobayashi and Zhao*, 2004; *Gupta et al.*, 2009] have been proposed. In this study we adopt one of the latter methods using the transformation from equatorial to ecliptic coordinates, which is proposed in the field of seismic waveform modeling (= quasi-Cartesian approach) [*Takenaka et al.*, 2017].

Consider that locations (longitude, latitude) of a reference point and an arbitrary point in the equatorial coordinates are represented by (γ', ε) and (α', δ), respectively (Figure 3a). Let the

position of the arbitrary point be (α, δ) when rotated by an angle ψ around the Earth's axis so that the reference point to be $(90°, \varepsilon)$ (Figure 3b). Then the following relations hold:

$$\begin{aligned} \psi &= 90° - \gamma', \\ \alpha &= \alpha' + \psi. \end{aligned} \tag{3}$$

Furthermore, when the following coordinate transformation is performed, the original coordinate system is transformed into another coordinate system where the positions of the reference and the arbitrary points are $(90°, 0°)$ and (λ, β), respectively (Figure 3c):

$$\begin{aligned} \lambda &= \tan^{-1}\left(\frac{\sin\delta\sin\varepsilon + \cos\delta\sin\alpha\cos\varepsilon}{\cos\delta\cos\alpha}\right), \\ \beta &= \sin^{-1}(\sin\delta\cos\varepsilon - \cos\delta\sin\alpha\sin\varepsilon). \end{aligned} \tag{3'}$$

These equations are the same as the ones that transform the equatorial coordinates into ecliptic coordinates. Therefore, the coordinates after the conversion are hereinafter referred to as "ecliptic coordinates" for convenience. In this study, the position of the station SUMG (−38.461°, 72.574°) in the center of the GrIS is defined as the reference point (γ', ε). Therefore, the above operation is equivalent to moving Greenland along the spherical surface and bringing the station SUMG to the equator so that its location becomes $(90°, 0°)$. Thus, after the transformation, even if the grid nodes are arranged at equal angular intervals in latitude and longitude, the horizontal distances between adjacent grids are almost equal in the entire study regions.

When it is necessary to put the calculation results back to the original equatorial coordinates, we conduct the inverse coordinate transformation. By applying the transformation on the same reference point as the forward transformation, an arbitrary point (λ, β) on the

ecliptic coordinates is moved back to a point (α', δ) on the equatorial coordinates with the following equations:

$$\begin{aligned} \alpha &= \tan^{-1}\left(\frac{-\sin\beta\sin\varepsilon + \cos\beta\sin\lambda\cos\varepsilon}{\cos\beta\cos\lambda}\right), \\ \delta &= \sin^{-1}(\sin\beta\cos\varepsilon + \cos\beta\sin\lambda\sin\varepsilon), \\ \psi &= 90° - \gamma', \\ \alpha' &= \alpha - \psi. \end{aligned} \tag{4}$$

For the locations of seismic stations and earthquake hypocenters, coordinate transformation is done before the tomographic inversion. This enables to conduct the tomography in the transformed coordinates with almost no changes in the programs for the equatorial coordinates.

2.3 Data

We use P-wave arrival times of local earthquakes and P-wave relative travel-time residuals of teleseismic events recorded by 34 seismometers of the GLISN network as data for the regional tomography. The data are collected in two ways: (1) extracting P-wave arrival time data of local and teleseismic events from the ISC-EHB catalog opened to public on a website of the International Seismological Center (ISC) (http://www.isc.ac.uk/), and (2) picking the P-wave relative travel-time residuals directly from the teleseismic waveforms by using the cross-correlation analysis. Details of the data collection are described below.

2.3.1 Data selected from the ISC-EHB catalog

The P-wave arrival time data are extracted from the ISC-EHB catalog through the following three steps.

1. All P-wave arrival time data from M ≥ 3 earthquakes observed at 30 GLISN stations during 1960−2014 are collected from the ISC-EHB catalog. Note that the remaining 5 stations in the GLISN network are not included in the catalog for this observation period.

2. Earthquakes that occurred in the latitude range of [55°, 85°] and the longitude range of [−95°, 20°] are extracted as local earthquakes. Since there are only a small number of earthquakes around Greenland, all earthquakes recorded at one or more stations in the study region are extracted. As a result, 1508 P-wave arrival times from 934 local events are obtained (Figure 4a). The magnitudes of the extracted earthquakes range from 3.1 to 6.8, with focal depths in a range of 0.1−49.4 km.

3. Earthquakes in the epicentral range of [30°, 100°] recorded at any station of the GLISN network are extracted as teleseismic events. At this stage, 54,809 earthquakes are extracted, so we further select events recorded at five or more stations. As a result, 35,871 P-wave arrival times from 5399 teleseismic events are obtained. The data are processed to get relative travel-time residuals using the theoretical travel times calculated for the IASP91 model [*Kennett and Engdahl,* 1991] and Equation (2). The magnitudes of the extracted earthquakes range from 3.4 to 9.1, with focal depths in a range of 0.0−651.1 km.

2.3.2 Data picked by the cross-correlation analysis

The P-wave relative travel-time residuals picked from teleseismic waveforms are obtained through the following three steps.

1. The ISC-EHB catalog is an integrated catalog of arrival-time data reported by various organizations all over the world, but it does not cover all stations in the GLISN network. As for the two-year period from January 1, 2012 to December 31, 2014 out of the period of the

ISC-EHB catalog described in Section 2.3.1 (1960−2014), we can obtain waveform data recorded by the GLISN network because the network had fully operated since 2012. We download vertical-component broadband seismograms recorded at 34 GLISN stations from IRIS/DMC (https://ds.iris.edu/ds/nodes/dmc/). The relative travel times are picked using the method described in Section 2.4. We download waveforms from 208 teleseismic events with M ≥ 6.0.

2. As for the period from January 1, 2015 to July 15, 2019 in which there are no data in the ISC-EHB catalog, we select all earthquakes with M ≥ 6.0 from the United States Geological Survey (USGS) website (https://www.usgs.gov/). Then we extract 472 events in the epicentral distance range of [20°, 120°] recorded at any station of the GLISN network, and download the waveform data from the IRIS/DMC. The relative travel times are picked in the same way as Step 1.

3. According to Step 1, 1908 P-wave relative travel-time residuals from 161 teleseismic events obtained from the ISC-EHB catalog are replaced with 3844 relative travel-time residuals picked by the cross-correlation analysis. After Step 2, we have additional 3729 relative travel-time residuals from 186 teleseismic events. Therefore, the number of P-wave relative travel-time residuals obtained by the cross-correlation analysis is 7573 from 347 events. The total number of teleseismic P-wave relative travel-time residuals combined with the data from the ISC-EHB catalog is 41,536 from 5585 events (Figure 4b).

2.3.3 Data extraction in the crustal correction

In the crustal correction process described in Section 2.5, the teleseismic data with relative travel-time residuals that exceed ±3 s before and after the correction are discarded. As a

result, the number of teleseismic events and the number of relative travel-time residuals are 5539 and 41,126 before the crustal correction, and 5539 and 41,027 after the correction, respectively. The final data set used for our regional tomography includes these teleseismic data integrated with the 1508 P-wave arrival time data from 934 local earthquakes obtained from the ISC-EHB catalog.

2.4 Picking of relative travel times

We pick the P-wave relative travel times from teleseismic events using the waveform cross-correlation method [*VanDecar and Crosson*, 1990; *Liu and Zhao*, 2016]. First, the vertical-component GLISN broadband seismograms for each event are downloaded from the IRIS/DMC. The selected events are those with M ≥ 6 in the epicentral distance range of $30° \leq \Delta \leq 100°$ from any station in the GLISN network. Then we correct the instrumental responses from the acquired data, convert them into velocity waveforms, and remove offsets and trends. We also unify the sampling frequency of all data to 20 sps and apply a bandpass filter of 10−100 s. The theoretical P-wave arrival times calculated for the IASP91 model [*Kennett and Engdahl*, 1991] is subtracted from the time axis to obtain a relative time series. Note that the theoretical P-wave arrival times are hereinafter set to zero for all waveforms. We then cut out the waveforms for each event from −10.00 s to +15.55 s so that the number of data points is 512, up-sample to 160 sps, and paste up with respect to the epicentral distances. The central waveform is defined as a reference waveform. We take the cross-correlation of each waveform with the reference waveform. For the ith event, we define that ${\Delta t_{ij}}^{\mathrm{CCF}}$ is the lag time that maximizes the correlation between jth waveform and the reference waveform, and that Δt_{0ij} is the time difference in starting points between the jth waveform and the reference waveform. The total travel-time

difference Δt_{ij} is then expressed as $\Delta t_{ij} = \Delta t_{0ij} + \Delta t_{ij}^{\mathrm{CCF}}$. Finally we obtain P-wave relative travel-time residuals by replacing t_{ij} in Eq. (2) with Δt_{ij}. Note that, when there are multiple seismographs at the same location, the data are reduced to have one seismograph per location (Table S1). Figure S1 shows an example of seismograms from one teleseismic event picked using the cross-correlation method.

2.5 Crustal correction

Since the teleseismic rays have low sensitivity inside the crust, the effect of crustal heterogeneity on travel times is better to be reduced using a known crustal structure model (= "crustal correction"). We apply the method of *Jiang et al.* [2009a, b, 2015] to conduct the crustal correction. First we calculate 41,536 teleseismic rays from 5585 earthquakes using a global 1-D structure model in which the upper and lower crusts of the IASP91 model [*Kennett and Engdahl*, 1991] are replaced by $V_P = 6.0$ km/s and $V_P = 6.67$ km/s. We cut out the segment of each ray from the station to a depth of 42 km. Since the calculation is performed with the flat Conrad and Moho discontinuities located at depths of 20 and 40 km, respectively, the ray segment refracts twice at the two discontinuities. We calculate the theoretical P-wave travel times for the ray segment T_{ij}^{1D}, where i and j are the event and station numbers, respectively. Next we obtain a local 1-D structure model beneath each GLISN station from the CRUST1.0 model [*Laske et al.*, 2013]. Note that the CRUST1.0 model is a quasi-3-D global crustal model that divides the whole Earth into 1° × 1° tiles in latitude and longitude, and gives an average 1-D surface structure model (layer thickness, density, Vp, and Vs) beneath each tile. Without changing the shape of the ray segment obtained using the global 1-D model, we calculate the ray length passing through each layer obtained using the CRUST1.0 model. By integrating the values obtained by dividing each ray length by the Vp of each layer, we obtain the theoretical travel time for the 3-D

surface structure T_{ij}^{3D}. Finally we obtain the crustal correction value for the travel time from the ith event to the jth station by

$$\Delta T_{ij}^{\text{crust}} = T_{ij}^{3D} - T_{ij}^{1D}. \quad (5)$$

Therefore, the absolute travel-time residual after the crustal correction is

$$t_{ij} = T_{ij}{}^{\text{OBS}} - T_{ij}{}^{\text{CAL}} - \Delta T_{ij}^{\text{crust}}. \quad (6)$$

The relative travel-time residuals used in the tomographic inversion can be obtained by substituting Eq. (6) into Eq. (2). Figures 5a and 5b show distributions of the relative travel-time residuals averaged at each station for all events before and after the crustal correction, respectively. In Iceland, where many active volcanoes exist, the delay in observed arrival time is more prominent after the correction. In contrast, the early arrivals are remarkable in northeastern Greenland after the correction.

2.6 Calculation specifications

We conducted seven tomographic inversions as shown in Table 1. Except for Case 5, we use horizontal grid nodes that fall in the range of latitude [−20°, 20°] and longitude [70°, 120°] at 2° intervals after the coordinate transformation (Figure S2a). The grid meshes in the vertical direction in Cases 1−4 are set at depths of 5, 20, 40, 60, 80, 100, 120, 140, 160, 190, 220, 250, 280, 310, 340, 370, 400, 430, 460, 490, 520, 550, 580, 610, 640, 670 and 700 km. The grid meshes in the depth direction in Cases 6 and 7 are set at depths of 750, 800, 850, 900, 950, 1000, 1050, 1100, 1150, 1200, 1250, 1300, 1350, 1400, 1450 and 1500 km, in addition to those as in

Cases 1-4. Therefore, the total number of grid nodes in Cases 1−4 is 21 (latitude) × 26 (longitude) × 27 (depth)= 14,742, whereas in Cases 6 and 7 it is 21 (latitude) × 26 (longitude) × 43 (depth)= 23,478.

In Case 5 without the coordinate transformation, we use horizontal grid nodes that fall in the range of latitude [54°, 86°] and longitude [−96°, 26°] at 2° intervals (Figure S2b). The grid distribution in the depth direction is the same as that in Cases 1−4. Thus, the total number of grid nodes is 17 (latitude) × 62 (longitude) × 27 (depth)= 28,458.

Comparing Cases 1−4 with Case 5, we can see that the number of grid nodes is doubled before the coordinate transformation, even though the horizontal angular grid interval and the grid distribution in the depth direction are the same. This is because the horizontal grid interval per 1° longitude is narrow before the coordinate transformation, and therefore the study region cannot be covered sufficiently without increasing the number of grid nodes. In other words, the number of grid nodes can be reduced by half by applying the coordinate transformation.

The 1-D initial Vp model used for the calculation is shown in Figure S3. The Conrad and Moho depths are fixed at 20 and 40 km, respectively. The initial Vp in the upper crust and the lower crust is set to 6.0 and 6.7 km/s, respectively. In all calculations, the damping parameter $\lambda_d = 40$ and the smoothing parameter $\lambda_s = 2 \times 10^{-4}$ are adopted. We do not conduct hypocenter relocation in all computations.

3 Resolution tests and results

We conducted many resolution tests including restoring resolution test (RRT) [*Zhao et al.*, 1992] and synthetic resolution test (SRT) to evaluate the adequacy of ray coverage and special resolution. To conduct the RRT, we highlight the patterns of the real tomographic result when

342 constructing the RRT input velocity model, i.e., at the grid nodes with the Vp anomalies > +0.8%
343 or < −0.8% in the real tomographic model, we put constant Vp anomalies of +3% or −3% for
344 making the RRT input model. The Vp anomalies at the other grid nodes are set to zero. Two
345 datasets for the RRT inversion are constructed by calculating the theoretical arrival times for this
346 input model followed by adding random errors with a standard deviation of 0.1 s or 0.2 s. To
347 conduct the SRT, we construct an input model with a −3% low-Vp anomaly distributed as band
348 in the NW-SE direction from central Greenland to Iceland. The low-Vp region exists only at
349 depths ≤ 250 km, and the velocity at all grid nodes is set to zero at greater depths. Dataset for the
350 SRT inversion is constructed by calculating the theoretical arrival times for this input model
351 followed by adding random errors (−0.2 to +0.2 s) with a standard deviation of 0.1 s.

352 Figure S4 shows map views of the RRT results using random errors with a standard
353 deviation of 0.1 s. Spot-like low-Vp or high-Vp regions in the input model arranged at short
354 distances sometimes tend to be connected in the output model (for example, low-Vp regions at a
355 depth of 220 km). However, both the spatial patterns and amplitudes of the input model can be
356 sufficiently recovered at all depths. Furthermore, we cannot see prominent fake structures that do
357 not exist in the input model, which indicates excellent resolution of the Case 1 results. Figure S5
358 shows map views of the RRT results using random errors with a standard deviation of 0.2 s. The
359 output results are almost the same as those when we use a standard deviation of 0.1 s. Therefore,
360 as for the current dataset, we can confirm that the structure in our study region can be solved
361 very robustly.

362 Figure S6 shows the SRT results. At depths ≤ 250 km, the input model is well recovered
363 at all depths. At depths of 280 km and 310 km, we can see leakage of the low-Vp in a wide
364 extent. However, at a depth of 340 km, the leakage beneath central Greenland disappears, and it

remains only at the ends of the input low-Vp region. The leakages at the northwest and southeast ends disappear at depths of 430 and 520 km, respectively. The leakage at the southeastern end continues a little deeper, but in Iceland, such an artificial effect is considered to be small because the low-Vp zone actually exists in this area from surface to the mantle transition zone (MTZ). As a result of this test, the leakage of the low-Vp beneath central Greenland is expected about 60 km at the maximum, and we found that the resolution in the depth direction of the Case 1 results is quite good.

4 Results

This section shows the results obtained by our regional tomography. The results of Case 1 are described in detail, whereas the other results are mentioned briefly.

4.1 Case 1: Depths ≤ 700 km, with the coordinate transformation and crustal correction

Figure S7 shows the seismic rays of the local and teleseismic earthquakes calculated in Case 1. The map views of the results are shown in Figure 6.

At depths of 5−190 km, the most prominent features are low-Vp anomalies beneath the Iceland and Jan Mayen volcanos, and a low-Vp anomaly extending from the Greenland Sea to central Greenland through the east coast of Greenland, which seems to join the low-Vp anomalies beneath the Iceland and Jan Mayen volcanos at its eastern part. The low-Vp anomaly extends toward the northwest at shallow depths (5−80 km), and appears to traverse Greenland from northwest to southeast. Other weak low-Vp anomalies can be found beneath western Svalbard and southern Greenland. The most prominent high-Vp anomaly is beneath the northeast coast of Greenland and its offshore areas. Areas beneath the Ellesmere Island and the Baffin Island are also imaged as weak high-Vp anomalies.

387 At depths of 250−370 km, the low-Vp anomaly beneath the inland Greenland suddenly
388 disappears, leaving only spot-like low-Vp anomalies beneath the Iceland and Jan Mayen
389 volcanos. The low-Vp anomaly beneath western Svalbard can also be seen as a spot at all depths.
390 The high-Vp anomaly off the northeast coast of Greenland extends further inland, and at depths
391 of 310−370 km, the high-Vp anomalies cover wide areas beneath the northern, central eastern,
392 and southern parts of Greenland. An interesting feature is that the high-Vp anomaly in
393 northeastern Greenland appears to be housed within the bend of the Mid-Atlantic Ridge.

394 In the MTZ at depths of 430−610 km, the low-Vp anomalies beneath Iceland and Jan
395 Mayen volcanoes are connected together. At depths of 490−520 km, the low-Vp anomaly
396 beneath western Svalbard also merges to it, forming a widespread low-Vp zones along the Mid-
397 Atlantic Ridge. The low-Vp beneath Svalbard appears to separate again at depths below 550 km.
398 The high-Vp beneath inland Greenland is not as noticeable as that in the upper mantle.

399 At depths of 640−700 km, the low-Vp anomaly beneath the Iceland and Jan Mayen
400 volcanoes becomes inconspicuous, but instead the low-Vp anomaly beneath western Svalbard
401 becomes prominent. We can also see a high-Vp anomaly running in the NW-SE direction
402 beneath inland Greenland, and another high-Vp anomaly beneath southern Greenland.

403 The vertical cross-sections are shown in Figs. 7 and 8. The 250-km depth line gives a
404 guideline to the maximum thickness of the Greenlandic lithosphere [*Conrad and Lithgow-*
405 *Bertelloni*, 2006]. Figure 7a shows sections in the N-S direction. The D-D', E-E', and F-F'
406 sections show remarkable low-Vp at depths ≤ 250 km from the center of Greenland to the east
407 coast. In the H-H' and I-I' sections through Iceland, Jan Mayen, and Svalbard, we can see
408 conduit-like low-Vp zones beneath the three areas in the upper mantle. These low-Vp conduits

appear to merge at the MTZ to form a widespread low-Vp region. Furthermore, the low-Vp region is divided into northern and southern portions by a high-Vp body off the northeast coast of Greenland; it appears that a weak low-Vp zone in Svalbard on the northern side and a strong low-Vp zone from Jan Mayen to Iceland on the southern side are clearly distinguished.

As for the sections in the E-W direction (Fig. 7b), the G-G' section passing through Iceland shows a thick low-Vp conduit from surface to the lower mantle whose thickness well corresponds to the aperture of surface volcanoes. Figure 8a contains sections in the NW-SE direction. In the C-C' and D-D' sections passing through the center of Iceland, it can be seen that the low-Vp zone near the ground surface is continuous from Iceland to inland Greenland. The low-Vp zone below Iceland extends from surface to the lower mantle, but when crossing the Denmark Strait, it suddenly becomes thinner (depths ≤ 250 km), and then extends northwestward to the center of Greenland with an almost constant thickness. In the northwest, the low-Vp zone weakens and appears to be shallower. Figure 8b shows cross-sections in the NE-SW direction.

The computation time for Case 1 was about 2 minutes on a PC. The root mean square (RMS) of the total travel-time residuals is 1.94 s for the initial 1-D Vp model, whereas it is reduced to 0.57 s for the final 3-D Vp model.

4.2 Case 2: Depths ≤ 700 km, with the coordinate transformation, local events only

The Case 2 results are shown in Figures S8−S10. When only the local earthquake data are used, only the high-Vp anomalies near the MTZ beneath Greenland are imaged. In addition, there are many masked areas due to sparse ray coverage around the surface of central Greenland. The epicentral distances of the local rays around Greenland is about 20−30°, so the seismic rays usually dive down to the MTZ and have less sensitivity near the surface. Also the rays do not

sufficiently crisscross in the vicinity of the Mid-Atlantic Ridge, which make the low-Vp beneath volcanos almost invisible.

4.3 Case 3: Depths ≤ 700 km, with the coordinate transformation, teleseismic events only

The Case 3 results are shown in Figures S11−S13. The overall features in the upper mantle are similar to those in Case 1, but there is a major difference that the low-Vp anomaly beneath central Greenland is barely visible. Also the separation of the low-Vp conduits beneath the Iceland and Jan Mayen volcanoes from surface to the MTZ is less clear than in Case 1. Taking the results of Cases 2 and 3 into account, we can say that the low-Vp zone beneath central Greenland cannot be imaged for either local events or teleseismic events alone, and it is visible only when the rays from both the local and teleseismic events crisscross each other.

4.4 Case 4: Depths ≤ 700 km, with the coordinate transformation, without the crustal correction

The Case 4 results are shown in Figures S14−S16. The general features of the results are similar to those of Case 1, but without the crustal correction, the amplitude of low-Vp zones beneath the Iceland and Jan Mayen volcanos becomes weaker due to much slight differences between observed and theoretical arrival times at the stations around these volcanoes.

In particular, the H-H' and I-I' sections in the N-S direction (Fig. S15a) show that the low-Vp anomaly beneath Svalbard, where there is no volcano, has larger amplitude than the low-Vp zone beneath the Jan Mayen volcano, which indicates that these results are not reliable. In addition, the D-D' and E-E' sections in the NW-SE direction (Fig. S16a) show that the connection between the low-Vp zones beneath the Iceland volcanos and inland Greenland is weaker than in Case 1.

4.5 Case 5: Depths ≤ 700 km, without the coordinate transformation, with the crustal correction

Figure S17 shows map views of the Case 5 results. At depths ≤ 250 km, we cannot see the wide low-Vp region that is imaged in Case 1, but can see only spot-like low-Vp areas just beneath the seismic stations, which tend to be elongated in the N-S direction along the meridian. Similar localization and distortion of the resulting patterns are observed at other depths, showing clear influence of the non-uniform lateral grid intervals. We can say that the equalization of grid intervals is a very effective way for computations in the high-latitude regions to obtain reliable results.

4.6 Case 6: Depths ≤ 1,500 km, with the coordinate transformation and crustal correction

Figure S18 shows map views of the Case 6 results. The resulting patterns at depths ≤ 700 km are almost the same as the Case 1 results, but the low-Vp region extending from the Iceland and Jan Mayen volcanoes to central Greenland is much weaker than that in Case 1. Also, the low-Vp zone beneath western Svalbard seems to be interrupted at depths of 460−610 km. At depths of 1050−1500 km beneath southwestern Greenland, there is no region with a large velocity anomaly in this case although many global tomography models show a common high-Vp region that seems to be a subducted slab body [*Shephard et al.*, 2016]. Therefore, Case 1 results are judged as better results in this study. When the study region becomes wider, it is very difficult to obtain correct results because the effect of heterogeneity outside the study region could not be sufficiently mitigated in the computation of the relative travel-time residuals.

4.7 Case 7: Depths ≤ 1,500 km, with the coordinate transformation, without the crustal correction

Figure S19 shows map views of the Case 7 results. As in Case 6, no significant velocity anomalies appear at depths of 1050−1500 km.

5 Discussion

5.1 Low-Vp anomaly beneath central Greenland (depth ≤ 250 km)

As mentioned in Section 1, the tomographic results of previous studies are highly controversial, with a large variation in the resulting patterns and no clear low-velocity regions near the surface.

In the regional tomography conducted in this study, a distinct low-Vp anomaly running in the NW-SE direction at depths ≤ 250 km beneath central Greenland is found. Figure 9 shows a comparison of our tomographic result at 5 km depth with the crustal heat flow distribution determined by *Martos et al.* [2018]. Figure 9a shows that the low-Vp region has a rather linear shape in the west, but it spreads wider on the east coast, forming a wedge shape. The distribution of hot springs on the east coast of Greenland corresponds to locations where the low-Vp amplitudes are larger. Furthermore, the low-Vp region and the high crustal heat-flow region (Fig. 9b) show spatially very high coincidence. For example, both the low-Vp and high heat-flow amplitudes are largest in the wedge-shaped region from central Greenland to the east coast, and decreases in the western part. The weak low-Vp amplitudes in southern Greenland also correspond well to the high crustal heat flow in this region. In Figure 9, ancient tracks of the Iceland plume estimated by the previous studies [*Morgan*, 1983; *Forsyth et al.*, 1986; *Cox and Hart*, 1986; *Müller et al.*, 1993; *Lawver and Müller*, 1994; *Brozena*, 1995; *Steinberger et al.*,

2004; *O'Neill et al.*, 2005; *Doubrovine et al.*, 2012; *Rogozhina et al.*, 2016] are also plotted. Although the tracks vary depending on the study, it generally crosses central Greenland in the NW-SE direction, which agrees very well with the low-Vp and the high crustal heat-flow regions.

This low-Vp region extends beneath the Greenland Sea and connects with the low-Vp regions beneath the Iceland and Jan Mayen volcanos. However, the low-Vp zone beneath the volcanos extends deeper to the MTZ, while the low-Vp zone beneath Greenland disappears at depths ≥ 250 km (Fig. 10), which show a clear difference between the two low-Vp zones. In particular, the cross sections clearly show that the low-Vp zone in the center of Greenland is distributed in a plate shape with a boundary at ~250 km depth. The RRT results indicate that the shape of the low-Vp zone at depths of 5−220 km is almost accurately recovered (Figs. S4 and S5). The SRT in which an input low-Vp anomaly is assigned only at depths ≤ 250 km shows that the depth range where the low-Vp leaks beyond a depth of 250 km is ~60 km beneath inland Greenland (Fig. S6). Therefore, even when the effect of leakage is taken into account in the tomographic results, the plate-like low-Vp zone is considered to exist from the surface to a depth of 200 km beneath central Greenland. Since the thickness of the Greenlandic lithosphere is estimated to be 200-230 km [*Conrad and Lithgow-Bertelloni*, 2006], the low-Vp zone in our tomography model is likely to exist only within the lithosphere.

Taken the above characteristics together, the low-Vp zone beneath central Greenland is considered to be due to the lithosphere, which is hotter than the surroundings. The heat might have been transmitted when the Greenlandic lithosphere was directly above the Iceland plume, and remained only in the lithosphere as it moved away from the plume due to the plate motion.

Our results show that the low-Vp region beneath central Greenland is also connected with the low-Vp spot beneath the Jan Mayen volcano. Since the Jan Mayen volcano is known as a

hotspot, it can be interpreted that the low-Vp track had also been formed by the similar mechanism as that for the Iceland plume. The low-Vp zone beneath Greenland narrows in the west and has a wedge-shaped spread in the east, which might be formed because only the Iceland plume was affected in the west but both the Iceland and Jan Mayen plumes were affected in the east. Such interpretation needs to be examined further, but it has a potential to constrain the interaction history between Greenland and the two plumes.

5.2 Volcanic and geothermal activities along the Mid-Atlantic Ridge

In our regional tomography, prominent conduit-like low-Vp zones are revealed beneath the Iceland and Jan Mayen volcanos, and western Svalbard. The Iceland and Jan Mayen volcanoes are known as hotspot volcanoes, but the low-Vp conduit that seems to be a plume beneath Svalbard is first discovered in this study. Western Svalbard is known as the high geothermal area [*Dumke et al.*, 2016], so the heat source might be this plume. We call this plume the Svalbard plume. Therefore, the Iceland volcanos, the Jan Mayen volcano, and the geothermal area in Svalbard are powered by the Iceland, Jan Mayen, and Svalbard plumes, respectively, which continue from the surface to the upper mantle (Fig. 10e). These three plumes merge together in the MTZ, forming a widespread low-Vp region.

A high-Vp body is visible beneath northeastern Greenland (Fig. 10b). The reason for the absence of volcanos in Svalbard might be because the rising of the Svalbard plume from the MTZ has been prevented by this body and sufficient magma is not supplied (Fig. 10e). The high-Vp body extends from the northeast coast of Greenland to the northeast offshore from surface to a depth of ~500 km. Because the rocks of the Caledonian orogen are widely distributed on the northeast coast of Greenland, this high-Vp body is thought to be similar rocks continuing to offshore. The Caledonian orogen was formed when the Iapetus Ocean located between Laurentia

and Baltica continents closed 490−390 million years ago [e.g., *Henriksen et al.*, 2009; *Metelkin et al.*, 2015]. Therefore, the high-Vp body revealed by our tomography might be the accumulation of oceanic lithosphere that constituted the Iapetas Ocean.

The Danmarkshavn Basin is located off the northeast coast of Greenland, which has thick sediments [*Henriksen et al.*, 2009, 74p]. Thick sediments suggest that the basement rocks in this area are heavier and settled than their surroundings, and reinforce that they are the remnants of marine lithosphere. As mentioned in Section 4, this high-Vp body is located inside the bend of the Mid-Atlantic Ridge (Figs. 10a and 10b). Since this bend is considered to have existed at the time of the Pangea breakup [*Thiede et al.*, 2011], the high-Vp body might have restricted the mode of plate expansion.

5.3 For melting prediction at the bottom of the GrIS

Rogozhina et al. [2016] suggested that in central and northern Greenland, high crustal heat-flow and the GrIS' own weight may cause widespread pressure melting at the bottom of the GrIS. This is reinforced by the direct observation of the bottom condition of the GrIS by the ice core drilling [*Dahl-Jensen et al.*, 2003a], and the analysis of the temporal change in surface-wave group velocity [*Toyokuni et al.*, 2018]. The average thickness of the GrIS is 2 km and reaches 3 km at its thickest point [*Bamber et al.*, 2001a,b], and when everything had melted due to the climate change, the global sea level is expected to rise by more than 7 m [*Houghton et al.*, 2001]. Melting from the ice sheet surface is currently monitored with sufficient accuracy by various remote-sensing techniques, but melting from the bottom is mainly predicted by temperature simulations [e.g., *MacGregor et al.*, 2016; *Rogozhina et al.*, 2016]. The heterogeneous structure of the crust and upper mantle used in the temperature simulation largely

depends on the results of seismic tomography. If a temperature simulation is performed using the results of this study, the prediction of ice sheet melting is expected to be more accurate.

6 Conclusions

A detailed 3-D P-wave velocity model from the surface to the MTZ beneath Greenland and surrounding regions is obtained by inverting a large number of high-quality P-wave arrival-time data of local earthquakes and P-wave relative travel-time residuals of teleseismic events recorded by the latest seismograph network. The novel tomographic model reveals the following new features.

(1) A remarkable low-Vp anomaly elongated in the NW-SE direction is revealed at depths ≤ 250 km beneath central Greenland, which may reflect the residual heat when the Greenlandic plate passed over the Iceland plume at ~80−20 Ma. Although previous studies have suggested this feature, our results first show that the low-Vp zone is within the lithosphere and its spatial distribution agrees very well with the high crustal heat-flow region. Furthermore, we find a possible heat track by the Jan Mayen plume.

(2) Prominent conduit-like low-Vp zones are revealed beneath the Iceland and Jan Mayen volcanos. Furthermore, the low-Vp conduit beneath western Svalbard that seems like a plume is first discovered in this study, which is called “the Svalbard plume”. Western Svalbard is known as a high geothermal area, so the heat might be powered by this plume. The three plumes beneath Iceland, Jan Mayen, and Svalbard merge together in the MTZ, forming a widespread low-Vp region.

(3) A high-Vp anomaly exists at depths ≤ 500 km off the northeast coast of Greenland, which is considered as a remnant of oceanic lithosphere that constituted the Iapetas Ocean. The

585 high-Vp body might be an obstacle for plume flow to provide sufficient magma to Svalbard.
586 Furthermore, it is located at the bend of the Mid-Atlantic Ridge and might have caused changes
587 in the plate-spreading direction, when Pangea started spreading.

588 **Acknowledgments**

589 We are grateful to Drs. Dean Childs, Kevin Nikolaus, Kent Anderson, Masaki Kanao,
590 Yoko Tono, Seiji Tsuboi, Robin Abbott, Kathy Young, Drew Abbott, Silver Williams, Jason
591 Hebert, Tetsuto Himeno, Susan Whitley, Orlando Leone, Akram Mostafanejad, Kirsten Arnell,
592 and other staff at GLISN, IRIS/PASSCAL, CH2M HILL Polar Services, and Norlandair for their
593 contributions to the field operations in Greenland. We thank the staffs of ISC, USGS, and
594 IRIS/DMC for providing the open-access arrival-time and waveform data archive. Dr. Yasmina
595 M. Martos kindly provided the heat flux data in Greenland and the data for plume track locations.
596 We also thank Dr. Árni Hjartarson for the location data of hot springs in Greenland. We
597 appreciate Drs. Hiroshi Takenaka, Akira Hasegawa, Satoshi Miura, Toru Matsuzawa, Ryota
598 Hino, Tomomi Okada, and Katsutada Kaminuma for helpful discussions. This work was partially
599 supported by research grants from Japan Society for the Promotion of Science (Nos. 15K17742,
600 18K03794, 24403006, 23224012, 26282105, and 26241010). The free software GMT [*Wessel et*
601 *al.*, 2013] and SAC [*Goldstein et al.*, 2003] are used in this study. Archiving of data from this
602 study is underway through Zenodo. Currently these data can be seen in Supporting Information
603 for review purposes. Part of the arrival-time data were downloaded from the International
604 Seismological Center (ISC) (http://www.isc.ac.uk/). The waveform data were downloaded from
605 the Data Management Center of the Incorporated Research Institutions for Seismology
606 (https://ds.iris.edu/ds/nodes/dmc/). Part of the event data were downloaded from the United
607 States Geological Survey (https://www.usgs.gov/).

Author contributions

G.T. and D.Z. designed this study. G.T. and T.M. conducted data processing and inversion. G.T. and T.M. wrote the manuscript. All authors contributed to the interpretations and preparation of the manuscript. G.T. contributed to the installation and maintenance of six GLISN stations including three on the GrIS. The authors declare that they have no competing interests.

References

Artemieva, I. M. (2019). Lithosphere thermal thickness and geothermal heat flux in Greenland from a new thermal isostasy method. *Earth-Science Reviews*, 188, 469–481. https://doi.org/10.1016/j.earscirev.2018.10.015

Bamber, J. L., Ekholm, S., & Krabill, W. B. (2001a). A new, high-resolution digital elevation model of Greenland fully validated with airborne laser altimeter data. *Journal of Geophysical Research: Solid Earth*, 106(B4), 6733–6745. http://dx.doi.org/10.1029/2000JB900365

Bamber, J. L., Layberry, R. L., & Gogineni, S. P. (2001b). A new ice thickness and bed data set for the Greenland ice sheet: 1. Measurement, data reduction, and errors. *Journal of Geophysical Research: Atmospheres*, 106(D24), 33773–33780. http://dx.doi.org/10.1029/2001JD900054

Braun, A., Kim, H. R., Csatho, B., von Frese, R. R. B. (2007). Gravity-inferred crustal thickness of Greenland. *Earth and Planetary Science Letters*, 262(1–2), 138-158. https://doi.org/10.1016/j.epsl.2007.07.050

Brozena, J.M. (1995). *Kinematic GPS and Aerogeophysical Measurement: Gravity, Topography and Magnetics*. PhD Thesis, University of Cambridge.

Clinton, J. F., Nettles, M., Walter, F., Anderson, K., Dahl-Jensen, T., Giardini, D., Govoni, A., Hanka, W., Lasocki, S., Lee, W. S., McCormack, D., Mykkeltveit, S., Stutzmann, E., & Tsuboi, S. (2014). Seismic network in Greenland monitors Earth and ice system. *Eos, Transactions, American Geophysical Union*, 95(2), 13–24. https://doi.org/10.1002/2014EO020001

Conrad, C. P., & Lithgow-Bertelloni, C. (2006). Influence of continental roots and asthenosphere on plate-mantle coupling. *Geophysical Research Letters*, 33, L05312. https://doi.org/10.1029/2005GL025621

Cox, A., & Hart, R. B. (1986). *Plate tectonics: How it works*, 418 pp. Oxford, UK: Blackwell Scientific Publications.

Dahl-Jensen, D., Gundestrup, N., Gogineni, S. P., & Miller, H. (2003a). Basal melt at NorthGRIP modeled from borehole, ice-core and radio-echo sounder observations. *Annals of Glaciology*, 37, 207–212. http://dx.doi.org/10.3189/172756403781815492

Dahl-Jensen, T., Larsen, T. B., Woelbern, I., Bach, T., Hanka, W., Kind, R., Gregersen, S., Mosegaard, K., Voss, P., & Gudmundsson, O. (2003b). Depth to Moho in Greenland: receiver-function analysis suggests two Proterozoic blocks in Greenland. *Earth and Planetary Science Letters*, 205(3–4), 379-393. https://doi.org/10.1016/S0012-821X(02)01080-4

Darbyshire, F. A., Larsen, T. B., Mosegaard, K., Dahl-Jensen, T., Gudmundsson, Ó., Bach, T., Gregersen, S., Pedersen, H. A., & Hanka, W. (2004). A first detailed look at the Greenland lithosphere and upper mantle, using Rayleigh wave tomography. *Geophysical*

Journal International, 158(1), 267–286. https://doi.org/10.1111/j.1365-246X.2004.02316.x

Darbyshire, F. A., Dahl-Jensen, T., Larsen, T. B., Voss, P. H., & Joyal, G. (2018). Crust and uppermost-mantle structure of Greenland and the Northwest Atlantic from Rayleigh wave group velocity tomography. *Geophysical Journal International*, 212(3), 1546–1569. https://doi.org/10.1093/gji/ggx479

Doubrovine, P. V., Steinberger, B., & Torsvik, T. H. (2012). Absolute plate motions in a reference frame defined by moving hotspots in the Pacific, Atlantic and Indian oceans. *Journal of Geophysical Ressearch: Solid Earth*, 117, B09101. https://doi.org/10.1029/2011JB009072

Dumke, I., Burwicz, E. B., Berndt, C., Klaeschen, D., Feseker, T., Geissler, W. H., & Sarkar, S. (2016). Gas hydrate distribution and hydrocarbon maturation north of the Knipovich Ridge, western Svalbard margin. *Journal of Geophysical Research: Solid Earth*, 121(3), 1405–1424. https://doi.org/10.1002/2015JB012083

Ekström, G., Nettles, M., & Abers, G. A. (2003). Glacial earthquakes. *Science*, 302(5645), 622–624. http://dx.doi.org/10.1126/science.1088057

Ekström, G., Nettles, M., & Tsai, V. C. (2006). Seasonality and increasing frequency of Greenland glacial earthquakes. *Science*, 311(5768), 1756–1758. http://dx.doi.org/10.1126/science.1122112

Forsyth, D. A., Morel-a-l'Huissier, P., Asudeh, I., & Green, A. G. (1986). Alpha ridge and Iceland-products of the same plume? *Journal of Geodynamics*, 6(1–4), 197–214. https://doi.org/10.1016/0264-3707(86)90039-6

673 Forsyth, D. A., Morel-a-l'Huissier, P., Asudeh, I., & Green, A. G. (1986). Alpha ridge and
674 Iceland-products of the same plume? *Journal of Geodynamics*, 6(1–4), 197–214.
675 https://doi.org/10.1016/0264-3707(86)90039-6

676 Goldstein, P., Dodge, D., Firpo, M., & Minner, L. (2003). SAC2000: Signal processing and
677 analysis tools for seismologists and engineers. In W. H. K. Lee, H. Kanamori, P. C.
678 Jennings, & C. Kisslinger (Eds.), *International Geophysics* (Vol. 81, pp. 1613–1614).
679 London: Academic Press.

680 Gupta, S., Zhao, D., & Rai, S. (2009). Seismic imaging of the upper mantle under the Erebus
681 hotspot in Antarctica. *Gondwana Research, 16*, 109-118.

682 Henriksen, N., Higgins, A. K., Kalsbeek, F., & Pulvertaft, T. C. R. (2009). *Greenland from*
683 *Archaean to Quaternary, Descriptive Text to the 1995 Geological Map of Greenland,*
684 *1:2 500 000*, 126 pp. Copenhagen: Geological Survey of Denmark and Greenland.
685 https://doi.org/10.1007/978-4-431-55360-1

686 Hjartarson, A., & Armannsson, H. (2010). *Geothermal research in Greenland*. Paper presented
687 at World Geothermal Congress 2010, Bali, Indonesia.

688 Houghton, J. T., Ding, Y., Griggs, D. J., Noguer, M., van der Linden, P. J., Dai, X., Maskell, K.,
689 & Johnson, C. A. (Eds.). (2001). *Climate Change 2001: The Scientific Basis*, 881pp.
690 Cambridge and New York: Cambridge Univ Press.

691 Jakovlev, A. V., Bushenkova, N. A., Koulakov, I. Yu., & Dobretsov, N. L. (2012). Structure of
692 the upper mantle in the Circum-Arctic region from regional seismic tomography. *Russian*
693 *Geology and Geophysics*, 53(10), 963–971. https://doi.org/10.1016/j.rgg.2012.08.001

694 Jiang, G., Zhao, D., & Zhang, G. (2009a). Seismic tomography of the Pacific slab edge under
695 Kamchatka. *Tectonophysics*, 465(1–4), 190–203.
696 https://doi.org/10.1016/j.tecto.2008.11.019

697 Jiang, G., Zhao, D., & Zhang, G. (2009b). Crustal correction in teleseismic tomography and its
698 application (in Chinese with English abstract). *Chinese Journal of Geophysics*, 52(6),
699 1508–1514. https://doi.org/10.3969/j.issn.0001-5733.2009.06.012

700 Jiang, G., Zhang, G., Zhao, D., Lü, Q., Li, H., & Li, X. (2015). Mantle dynamics and Cretaceous
701 magmatism in east-central China: Insight from teleseismic tomograms. *Tectonophysics*,
702 664, 256–268. https://doi.org/10.1016/j.tecto.2015.09.019

703 Kennett, B. L. N., & Engdahl, E. R. (1991). Traveltimes for global earthquake location and phase
704 identification. *Geophysical Journal International*, 105: 429–465.
705 https://doi.org/10.1111/j.1365-246X.1991.tb06724.x

706 Kobayashi, R., & Zhao, D. (2004). Rayleigh-wave group velocity distribution in the Antarctic
707 region. *Physics of the Earth and Planetary Interiors*, 141(3), 167–181.
708 https://doi.org/10.1016/j.pepi.2003.11.011

709 Laske, G., Masters., G., Ma, Z., & Pasyanos, M. (2013). Update on CRUST1.0 - A 1-degree
710 global model of Earth's crust, *Geophysical Research Abstracts*, 15, Abstract EGU2013-
711 2658. https://meetingorganizer.copernicus.org/EGU2013/EGU2013-2658.pdf

712 Lawver, L. A., & Müller, R. D. (1994). Iceland hotspot track. *Geology*, 22(4), 311–314.
713 https://doi.org/10.1130/0091-7613(1994)022<0311:IHT>2.3.CO;2

714 Lebedev, S., Schaeffer, A. J., Fullea, J., & Pease, V. (2017). Seismic tomography of the Arctic
715 region: inferences for the thermal structure and evolution of the lithosphere. *Geological*
716 *Society, London, Special Publications*, 460, 419–440. https://doi.org/10.1144/SP460.10

717 Levshin, A. L., Shen, W., Barmin, M. P., & Ritzwoller, M. H. (2017). Surface wave studies of
718 the Greenland upper lithosphere using ambient seismic noise.
719 https://pdfs.semanticscholar.org/977c/ce2101b7f9b384d38e9b051bf289a7277b54.pdf

720 Liu, X., & Zhao, D. (2016). P and S wave tomography of Japan subduction zone from joint
721 inversions of local and teleseismic travel times and surface-wave data. *Physics of the*
722 *Earth and Planetary Interiors*, 252, 1–22. http://dx.doi.org/10.1016/j.pepi.2016.01.002

723 MacGregor, J. A., Colgan, W. T., Fahnestock, M. A., Morlighem, M., Catania, G. A., Paden, J.
724 D., & Gogineni, S. P. (2016). Holocene deceleration of the Greenland Ice Sheet. *Science*,
725 351(6273), 590–593. http://dx.doi.org/10.1126/science.aab1702

726 Martos, Y. M., Jordan, T. A., Catalán, M., Jordan, T. M., Bamber, J. L., & Vaughan, D. G.
727 (2018). Geothermal heat flux reveals the Iceland hotspot track underneath Greenland.
728 *Geophysical Research Letters*, 45, 8214– 8222. https://doi.org/10.1029/2018GL078289

729 Matthews, K. J., Maloney, K. T., Zahirovic, S., Williams, S. E., Seton, M., & Müller, R. D.
730 (2016). Global plate boundary evolution and kinematics since the late Paleozoic, *Global*
731 *and Planetary Change*, 146, 226-250. https://doi.org/10.1016/j.gloplacha.2016.10.002

732 Metelkin, D. V., Vernikovsky, V. A., Matushkin, N. Yu. (2015). Arctida between Rodinia and
733 Pangea. *Precambrian Research*, 259, 114–129.
734 https://doi.org/10.1016/j.precamres.2014.09.013

735 Mordret, A., Mikesell, T. D., Harig, C., Lipovsky, B. P., & Prieto, G. A. (2016). Monitoring
736 southwest Greenland's ice sheet melt with ambient seismic noise. *Science Advances*,
737 2(5), e1501538. http://dx.doi.org/10.1126/sciadv.1501538

738 Morgan, W. J. (1983). Hotspot tracks and the early rifting of the Atlantic. *Tectonophysics*, 94(1–
739 4), 123–139. https://doi.org/10.1016/0040-1951(83)90013-6

740 Müller, R. D., Royer, J. Y., & Lawver, L. A. (1993). Revised plate motions relative to the
741 hotspots from combined Atlantic and Indian Ocean hotspot tracks. *Geology*, 21(3), 275–
742 278. https://doi.org/10.1130/0091-7613(1993)021<0275:RPMRTT>2.3.CO;2

743 O'Neill, C., Müller, R. D., & Steinberger, B. (2005). On the uncertainties in hotspot
744 reconstructions, and the significance of moving hotspot reference frames. *Geochemistry,*
745 *Geophysics, Geosystems*, 6, Q04003. https://doi.org/10.1029/2004GC000784

746 Paige, C. C., & Saunders, M. A. (1982). LSQR, An algorithm for sparse linear equations and
747 sparse least squares. *ACM Transactions on Mathematical Software (TOMS)*, 8(1), 43–71.
748 https://doi.org/10.1145/355984.355989

749 Pilidou, S., Priestley, K., Gudmundsson, Ó., & Debayle, E. (2004). Upper mantle S-wave speed
750 heterogeneity and anisotropy beneath the North Atlantic from regional surface wave
751 tomography: the Iceland and Azores plumes. *Geophysical Journal International*, 159,
752 1057–1076. https://doi.org/10.1111/j.1365-246X.2004.02462.x

753 Pourpoint, M., Anandakrishnan, S., Ammon, C. J., & Alley, R. B. (2018). Lithospheric structure
754 of Greenland from ambient noise and earthquake surface wave tomography. *Journal of*
755 *Geophysical Research: Solid Earth*, 123, 7850–7876.
756 https://doi.org/10.1029/2018JB015490

Rickers, F., Fichtner, A., & Trampert, J. (2013). The Iceland–Jan Mayen plume system and its impact on mantle dynamics in the North Atlantic region: Evidence from full-waveform inversion. *Earth and Planetary Science Letters*, 367, 39–51. https://doi.org/10.1016/j.epsl.2013.02.022

Rogozhina, I., Petrunin, A. G., Vaughan, A. P. M., Steinberger, B., Johnson, J. V., Kaban, M. K., Calov, R., Rickers, F., Thomas, M., & Koulakov, I. (2016). Melting at the base of the Greenland ice sheet explained by Iceland hotspot history. *Nature Geoscience*, 9, 366–369. http://dx.doi.org/10.1038/ngeo2689

Shephard, G. E., Trønnes, R. G., Spakman, W., Panet, I., & Gaina, C. (2016). Evidence for slab material under Greenland and links to Cretaceous High Arctic magmatism. *Geophysical Research Letters*, 43(8), 3717–3726. https://doi.org/10.1002/2016GL068424

Steinberger, B., Sutherland, R., & O'Connell, R. J. (2004). Prediction of Emperor-Hawaii seamount locations from a revised model of plate motion and mantle flow. *Nature*, 430(6996), 167–173. https://doi.org/10.1038/nature02660

Takenaka, H., Komatsu, M., Toyokuni, G., Nakamura, T., & Okamoto, T. (2017). Quasi-Cartesian finite-difference computation of seismic wave propagation for a three-dimensional sub-global model. *Earth, Planets and Space*, 69, 67. https://doi.org/10.1186/s40623-017-0651-1

Thiede, J., Eldholm, O., & Myhre, A. M. (2011). Chapter 46 Scientific deep-sea drilling in high northern latitudes. *Geological Society, London, Memoirs*, 35, 703–714. https://doi.org/10.1144/M35.46

778 Toyokuni, G., Kanao, M., Tono, Y., Himeno, T., Tsuboi, S., Childs, D., Anderson, K., &
779 Takenaka, H. (2014). Monitoring of the Greenland ice sheet using a broadband
780 seismometer network: the GLISN project. *Antarctic Record*, 58(1), 1–18.
781 http://doi.org/10.15094/00009722

782 Toyokuni, G., Takenaka, H., Takagi, R., Kanao, M., Tsuboi, S., Tono, Y., Childs, D., & Zhao, D.
783 (2018). Changes in Greenland ice bed conditions inferred from seismology. *Physics of*
784 *the Earth and Planetary Interiors*, 277, 81–98. https://doi.org/10.1016/j.pepi.2017.10.010

785 Um, J., & Thurber, C. (1987). A fast algorithm for two-point seismic ray tracing. *Bulletin of the*
786 *Seismological Society of America*, 77(3), 972–986.

787 VanDecar, J. C., & Crosson, R. S. (1990). Determination of teleseismic relative phase arrival
788 times using multi-channel cross-correlation and least squares. *Bulletin of the*
789 *Seismological Society of America*, 80(1), 150–169.

790 Wessel, P., Smith, W. H. F., Scharroo, R., Luis, J., & Wobbe, F. (2013). Generic Mapping Tools:
791 Improved Version Released. *Eos, Transactions, American Geophysical Union*, 94(45),
792 409. https://doi.org/10.1002/2013EO450001

793 Zhao, D. (2015). *Multiscale Seismic Tomography*, 304 pp. Tokyo: Springer.
794 https://doi.org/10.1007/978-4-431-55360-1

795 Zhao, D. (2001). Seismic structure and origin of hotspots and mantle plumes. *Earth and*
796 *Planetary Science Letters*, 192(3), 251–265. https://doi.org/10.1016/S0012-
797 821X(01)00465-4

798 Zhao, D. (2004). Global tomographic images of mantle plumes and subducting slabs: insight into
799 deep Earth dynamics. *Physics of the Earth and Planetary Interiors*, 146(1–2), 3–34.
800 https://doi.org/10.1016/j.pepi.2003.07.032

801 Zhao, D. (2009). Multiscale seismic tomography and mantle dynamics. *Gondwana Research*,
802 15(3–4), 297–323. https://doi.org/10.1016/j.gr.2008.07.003

803 Zhao, D., Hasegawa, A., & Horiuchi, S. (1992). Tomographic imaging of P and S wave velocity
804 structure beneath northeastern Japan. *Journal of Geophysical Research*, 97(B13), 19909–
805 19928. https://doi.org/10.1029/92JB00603

806 Zhao, D., Hasegawa, A., & Kanamori, H. (1994). Deep structure of Japan subduction zone as
807 derived from local, regional, and teleseismic events. *Journal of Geophysical Research:*
808 *Solid Earth*, 99(B11), 22313–22329. https://doi.org/10.1029/94JB01149

809 Zhao, D., Yanada, T., Hasegawa, A., Umino, N., & Wei, W. (2012). Imaging the subducting
810 slabs and mantle upwelling under the Japan Islands. *Geophysical Journal International*,
811 190(2), 816–828. https://doi.org/10.1111/j.1365-246X.2012.05550.x

812

Figure 1. Greenland and its surrounding regions. The color scale for altitude and legends for symbols are shown in the map. The white color denotes the Greenland ice sheet (GrIS). Red triangles: active volcanoes; red circles: hot springs; yellow triangles: GLISN seismic stations.

Figure 2. Distribution of the GLISN stations. The background colors indicate the thickness of the GrIS [*Bamber et al.*, 2001a,b].

Figure 3. Schematic diagram of the coordinate transformation used in this study [*Takenaka et al.*, 2017]. **(a)** Before transformation. The position (longitude, latitude) of the reference point and an arbitrary point in the target region are set as (γ', ε) and (α', δ), respectively. **(b)** The first stage of the transformation. The coordinates is rotated around the Earth's axis so that the position of the reference point becomes $(90°, \varepsilon)$. **(c)** The second stage of the transformation. The coordinates is rotated so that the position of the reference point becomes $(90°, 0°)$.

Figure 4. Epicentral distribution of **(a)** 934 local earthquakes (yellow stars) and **(b)** teleseismic events used in this study. Red circles: 5213 events from the ISC catalog. Yellow stars: 347 events whose arrival times are picked by the authors using a waveform cross-correlation method. The blue lines denote the plate boundaries.

Figure 5. Distribution of averaged relative travel-time residuals at each station used in this study **(a)** before and **(b)** after the crustal correction (see text for details). Diamond and circle symbols denote early and delayed arrivals, respectively.

Figure 6. Map views of Case 1 results (the model bottom depth = 700 km, with the coordinate transformation and the crustal correction). The layer depth is shown at the lower-right corner of each map. The blue and red colors denote high and low P-wave velocity perturbations,

834 respectively, whose scale (in %) is shown on the right. Areas with hit counts < 5 are masked in
835 white. The red triangles, red circles, black inverted triangles, and thin black lines denote the
836 active volcanoes, hot springs, seismic stations, and plate boundaries, respectively.

837 **Figure 7**. Vertical cross-sections of Case 1 results along **(a)** nine profiles in the N-S direction
838 and **(b)** nine profiles in the E-W direction. Location of the profiles are shown on the inset map.
839 The 250-km depth, the 410-km discontinuity, and the 660-km discontinuity are shown in black
840 solid lines. The thick black lines on the surface denote land areas. Other labels are the same as
841 those in Figure 6.

842 **Figure 8**. The same as Fig. 7 but along **(a)** seven profiles in the NW-SE direction and **(b)** seven
843 profiles in the NE-SW direction.

844 **Figure 9**. Comparison of the seismic velocity structure and crustal heat flow. **(a)** P-wave velocity
845 tomography at 5 km depth obtained in this study. **(b)** Crustal heat flow from *Martos et al.* [2018].
846 The color lines denote the ancient tracks of the Iceland plume estimated by previous studies as
847 shown on the right.

848 **Figure 10**. Map views and vertical cross-sections showing main tectonic features in the study
849 region. Map views at **(a)** 80 km and **(b)** 310 km depths. The symbols are the same as those in Fig.
850 6. **(c–e)** Vertical cross-sections along three profiles as shown in the map views. The symbols are
851 the same as those in Figs. 7 and 8.

852 **Figure S1**. An example of waveforms from a teleseismic event picked using the cross-
853 correlation analysis. The event information (event number, origin time, hypocentral location, and
854 magnitude) is shown at the top. The left column shows the waveforms displayed with the

855 theoretical P-wave arrival time as zero, and arranged in order of epicentral distance. We choose
856 the waveform observed at the middle of the epicentral distances as a reference waveform. The
857 right column shows the same waveforms shifted in time by subtracting the relative travel times
858 with respect to the reference waveform. The station codes and epicentral distances are shown on
859 the right. A bandpass filter of 10−100 s is applied to all the waveforms. See text for details.

860 **Figure S2**. Horizontal grid distribution for tomography **(a)** with and **(b)** without the coordinate
861 transformation. The blue triangles denote the GLISN stations.

862 **Figure S3**. The starting 1-D P-wave velocity model adopted for 3-D tomographic inversions.

863 **Figure S4**. Map views of the input (upper panels) and output (lower panels) models of the
864 restoring resolution test (RRT; see the text for details). Random noise (-0.2 to +0.2 s) with a
865 standard deviation of 0.1 s is added to the synthetic data before the tomographic inversion. The
866 layer depth is shown above each map. The labels are the same as those in Figure 6.

867 **Figure S5**. The same as Fig. S4 but for the restoring resolution test (RRT; see the text for details).
868 Random noise (-0.4 to +0.4 s) with a standard deviation of 0.2 s is added to the synthetic data
869 before the tomographic inversion.

870 **Figure S6**. The same as Fig. S4 but for the synthetic resolution test (SRT; see the text for details).
871 Random noise (-0.2 to +0.2 s) with a standard deviation of 0.1 s is added to the synthetic data
872 before the tomographic inversion.

873 **Figure S7**. Distribution of seismic rays in the study region for Case 1. For **(a)** local and **(b)**
874 teleseismic events.

875 **Figure S8**. The same as Fig. 6 but for Case 2 (the model bottom depth = 700 km, with the
876 coordinate transformation, only the local earthquake data are used).

877 **Figure S9**. The same as Fig. 7 but for Case 2.

878 **Figure S10**. The same as Fig. 8 but for Case 2.

879 **Figure S11**. The same as Fig. 6 but for Case 3 (the model bottom depth =700 km, with the
880 coordinate transformation and the crustal correction, only the teleseismic data are used).

881 **Figure S12**. The same as Fig. 7 but for Case 3.

882 **Figure S13**. The same as Fig. 8 but for Case 3.

883 **Figure S14**. The same as Fig. 6 but for Case 4 (the model bottom depth = 700 km, with the
884 coordinate transformation but without the crustal correction).

885 **Figure S15**. The same as Fig. 7 but for Case 4.

886 **Figure S16**. The same as Fig. 8 but for Case 4.

887 **Figure S17**. The same as Fig. 6 but for Case 5 (the model bottom depth = 700 km, without the
888 coordinate transformation but with the crustal correction).

889 **Figure S18**. The same as Fig. 6 but for Case 6 (the model bottom depth = 1500 km, with the
890 coordinate transformation and the crustal correction).

891 **Figure S19**. The same as Fig. 6 but for Case 7 (the model bottom depth = 1500 km, with the
892 coordinate transformation but without the crustal correction).

893 **Table 1.** Information on the seven tomographic inversions conducted by this study.

894 **Table S1.** List of 34 seismic stations of the GLISN network.

895

896

897

898

899

900

901

902

903

904

905

906

907

908

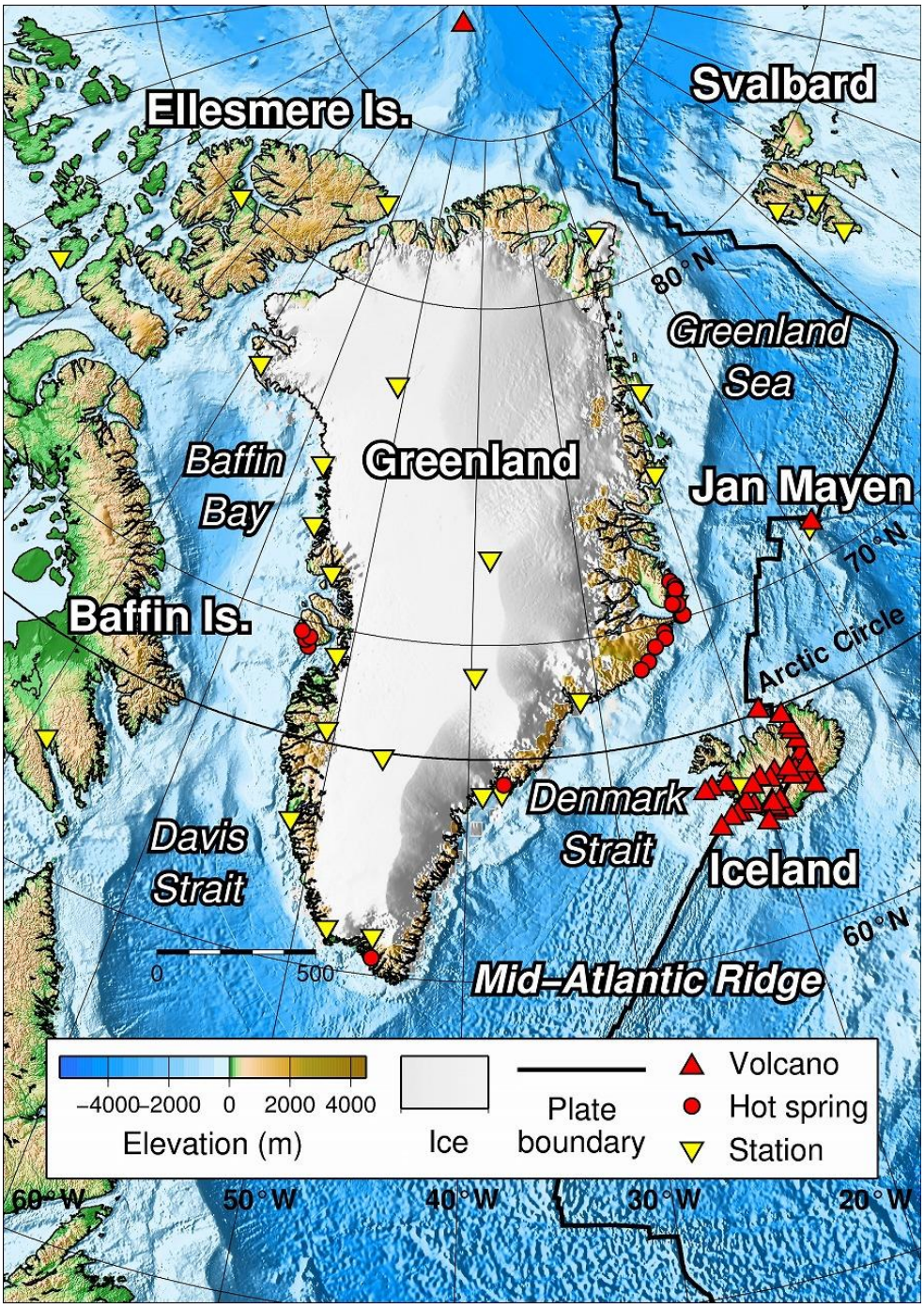

Figure 1. Greenland and its surrounding regions. The color scale for altitude and legends for symbols are shown in the map. The white color denotes the Greenland ice sheet (GrIS). Red triangles: active volcanoes; red circles: hot springs; yellow triangles: GLISN seismic stations.

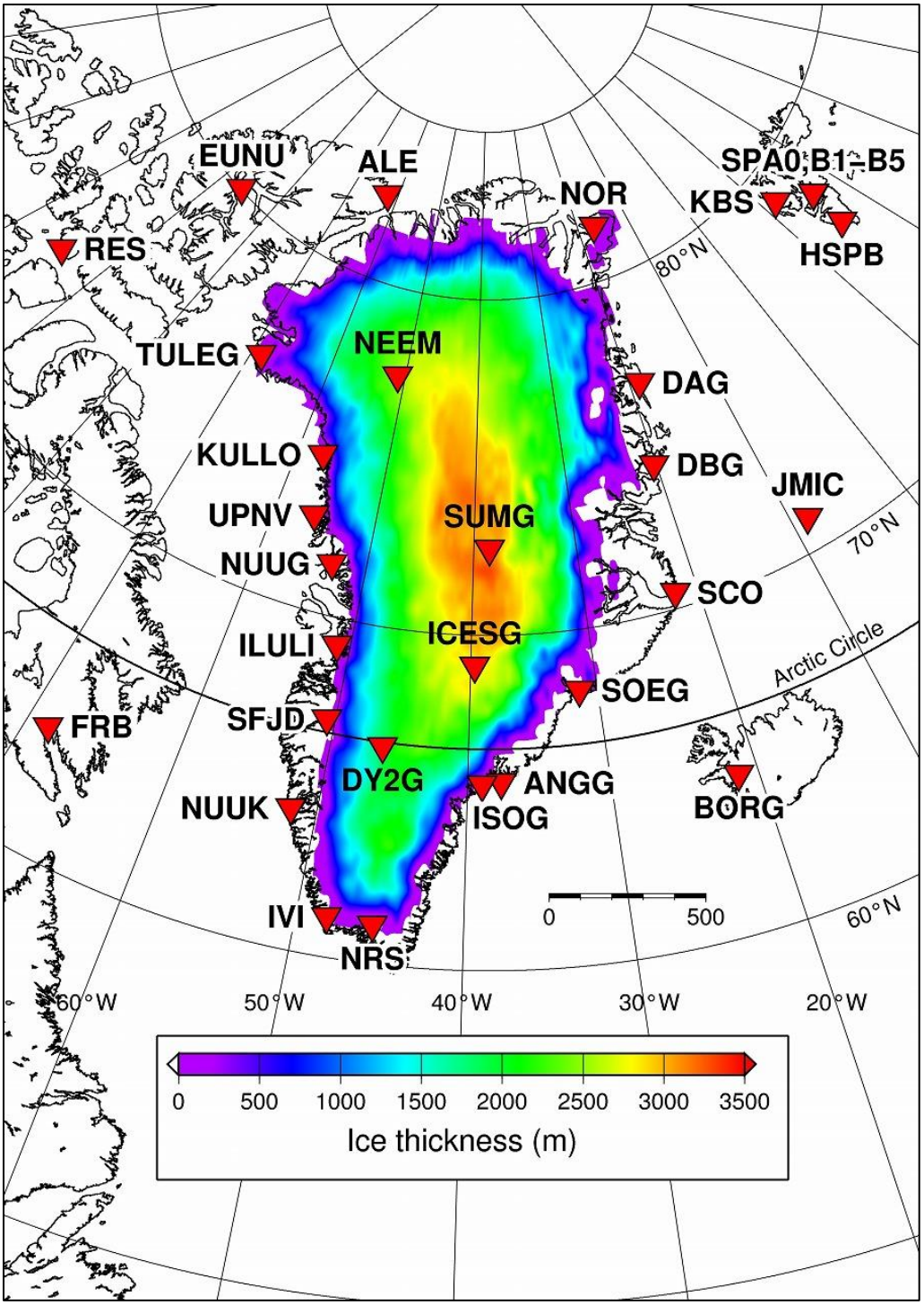

913

914 **Figure 2**. Distribution of the GLISN stations. The background colors indicate the thickness of

915 the GrIS [*Bamber et al.*, 2001a,b].

916

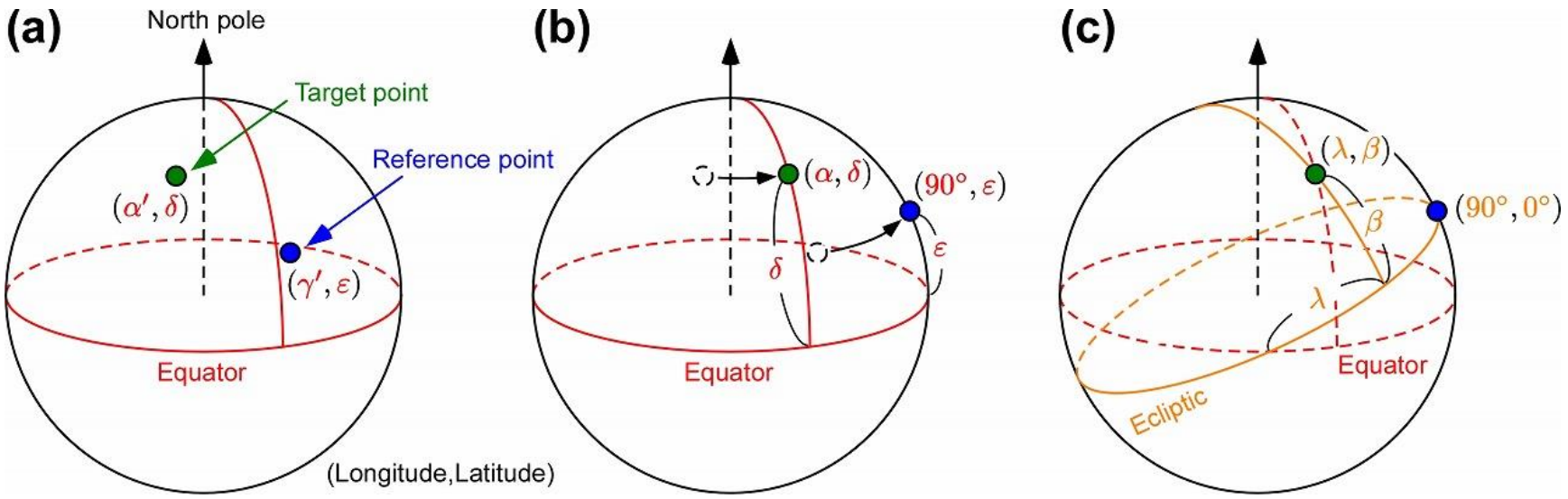

Figure 3. Schematic diagram of the coordinate transformation used in this study [*Takenaka et al.*, 2017]. **(a)** Before transformation. The position (longitude, latitude) of the reference point and an arbitrary point in the target region are set as (γ', ε) and (α', δ), respectively. **(b)** The first stage of the transformation. The coordinates is rotated around the Earth's axis so that the position of the reference point becomes $(90°, \varepsilon)$. **(c)** The second stage of the transformation. The coordinates is rotated so that the position of the reference point becomes $(90°, 0°)$.

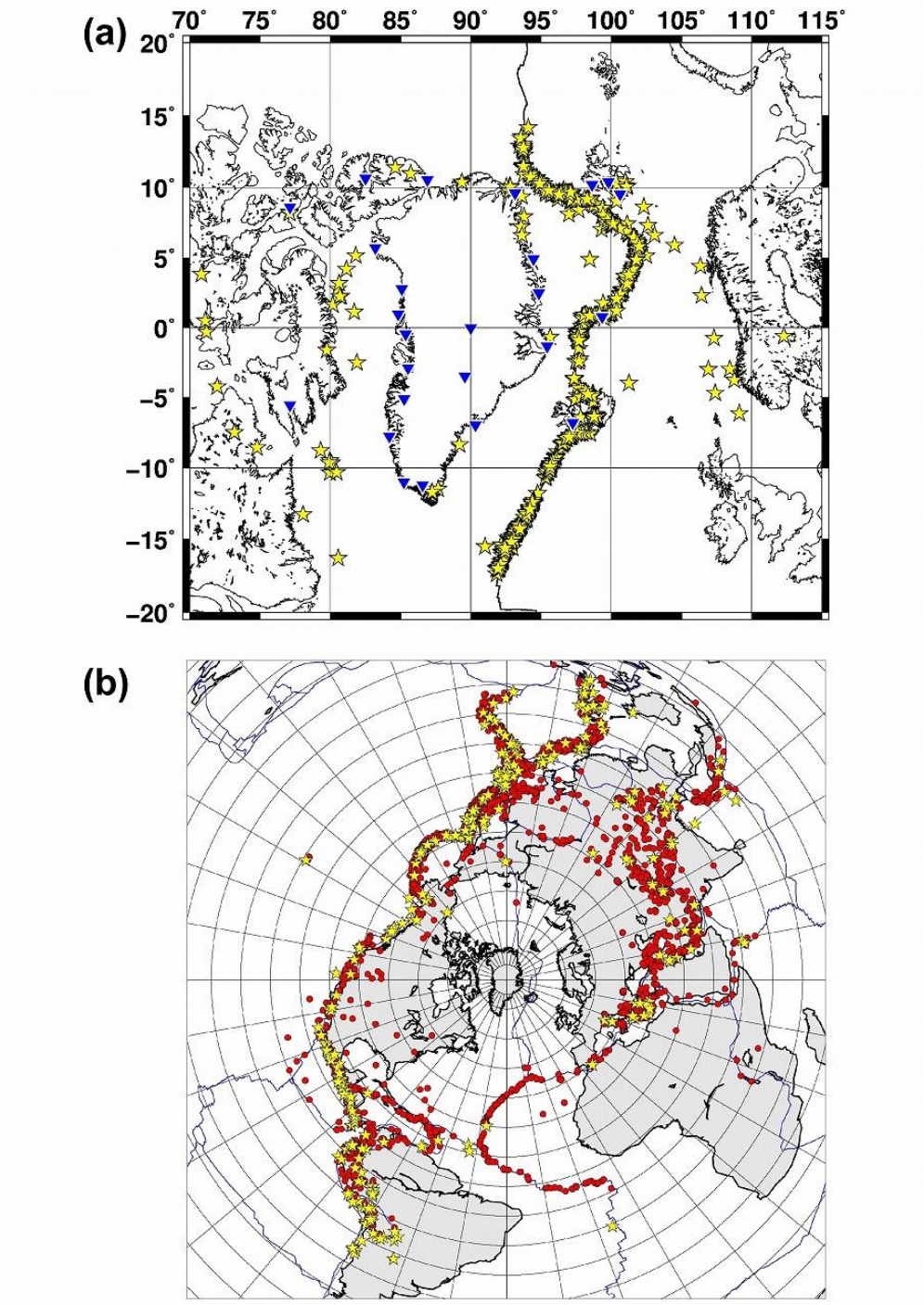

926

927 **Figure 4**. Epicentral distribution of **(a)** 934 local earthquakes (yellow stars) and **(b)** teleseismic

928 events used in this study. Red circles: 5213 events from the ISC catalog. Yellow stars: 347

929 events whose arrival times are picked by the authors using a waveform cross-correlation method.

930 The blue lines denote the plate boundaries.

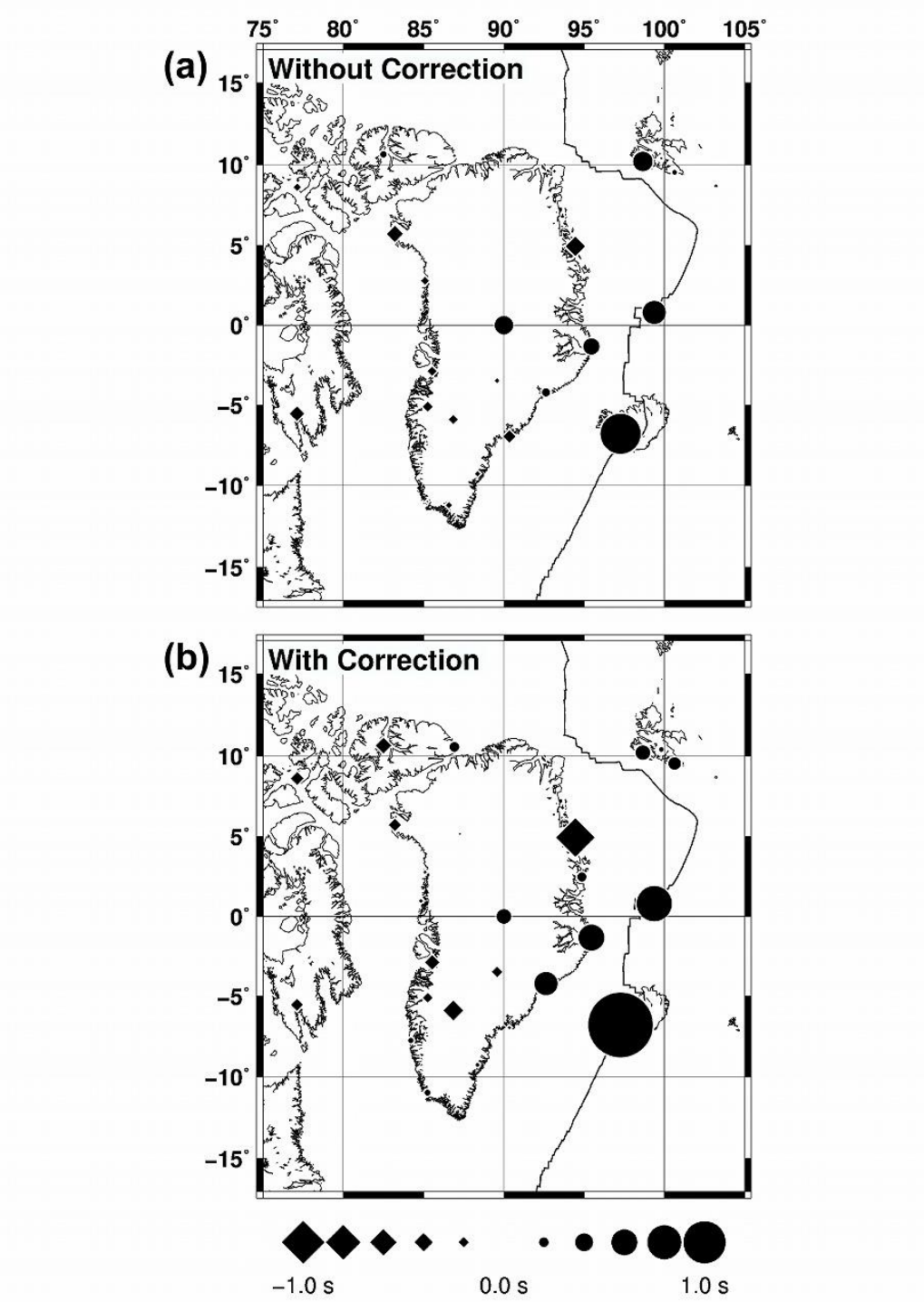

931

932 **Figure 5**. Distribution of averaged relative travel-time residuals at each station used in this study

933 **(a)** before and **(b)** after the crustal correction (see text for details). Diamond and circle symbols

934 denote early and delayed arrivals, respectively.

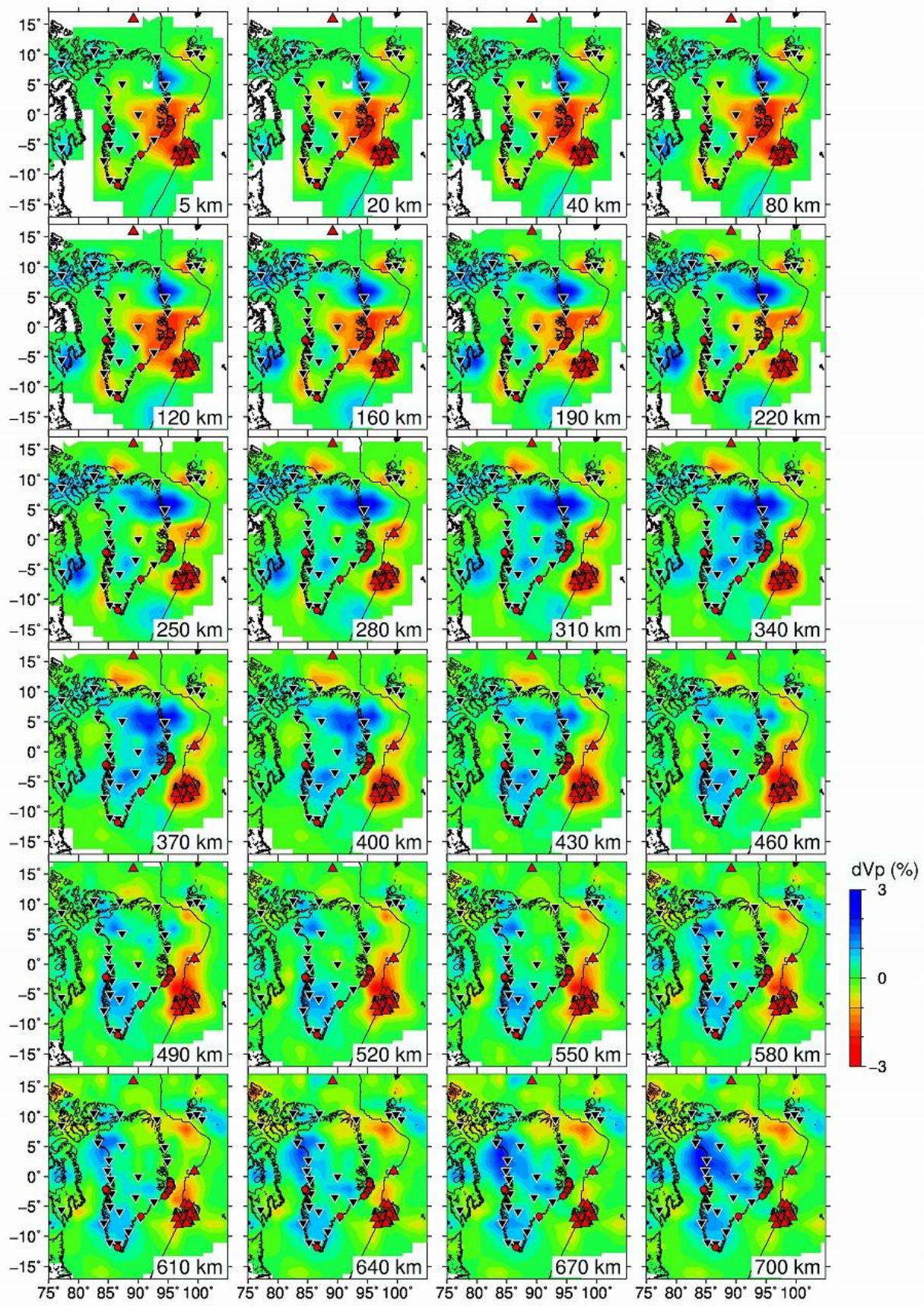
5 km
20 km
40 km
80 km
120 km
160 km
190 km
220 km
250 km
280 km
310 km
340 km
370 km
400 km
430 km
460 km
490 km
520 km
550 km
580 km
610 km
640 km
670 km
700 km
15°
10°
5°
0°
−5°
−10°
−15°
75° 80° 85° 90° 95° 100°
dVp (%)
3
0
−3

935

Figure 6. Map views of Case 1 results (the model bottom depth = 700 km, with the coordinate transformation and the crustal correction). The layer depth is shown at the lower-right corner of each map. The blue and red colors denote high and low P-wave velocity perturbations, respectively, whose scale (in %) is shown on the right. Areas with hit counts < 5 are masked in white. The red triangles, red circles, black inverted triangles, and thin black lines denote the active volcanoes, hot springs, seismic stations, and plate boundaries, respectively.

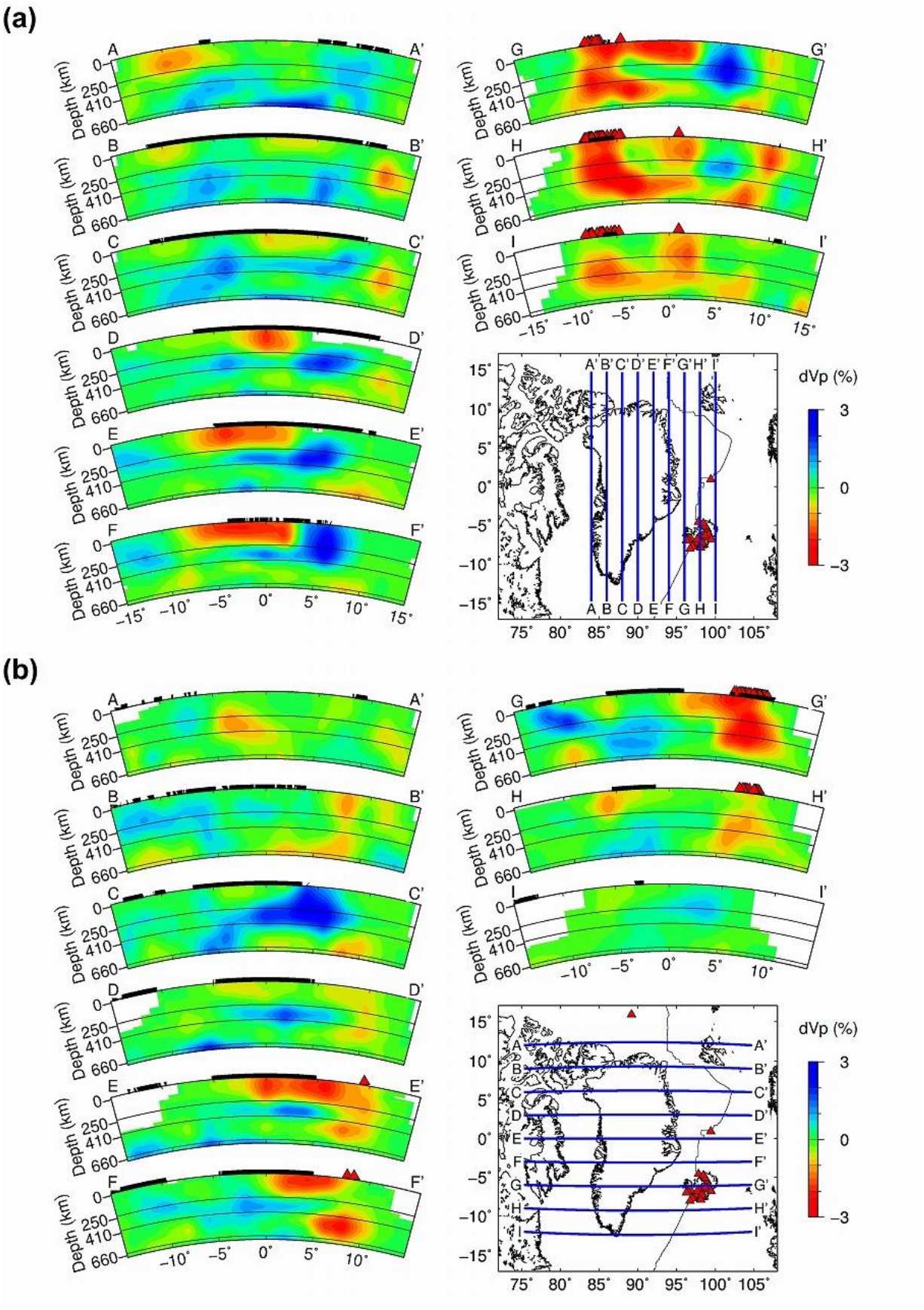
(a)
(b)
Depth (km)
0
250
410
660
dVp (%)
3
0
−3
75° 80° 85° 90° 95° 100° 105°
15° 10° 5° 0° −5° −10° −15°

959

960 **Figure 7**. Vertical cross-sections of Case 1 results along **(a)** nine profiles in the N-S direction
961 and **(b)** nine profiles in the E-W direction. Location of the profiles are shown on the inset map.
962 The 250-km depth, the 410-km discontinuity, and the 660-km discontinuity are shown in black
963 solid lines. The thick black lines on the surface denote land areas. Other labels are the same as
964 those in Figure 6.
965
966
967
968
969
970
971
972
973
974
975
976
977
978
979
980
981
982

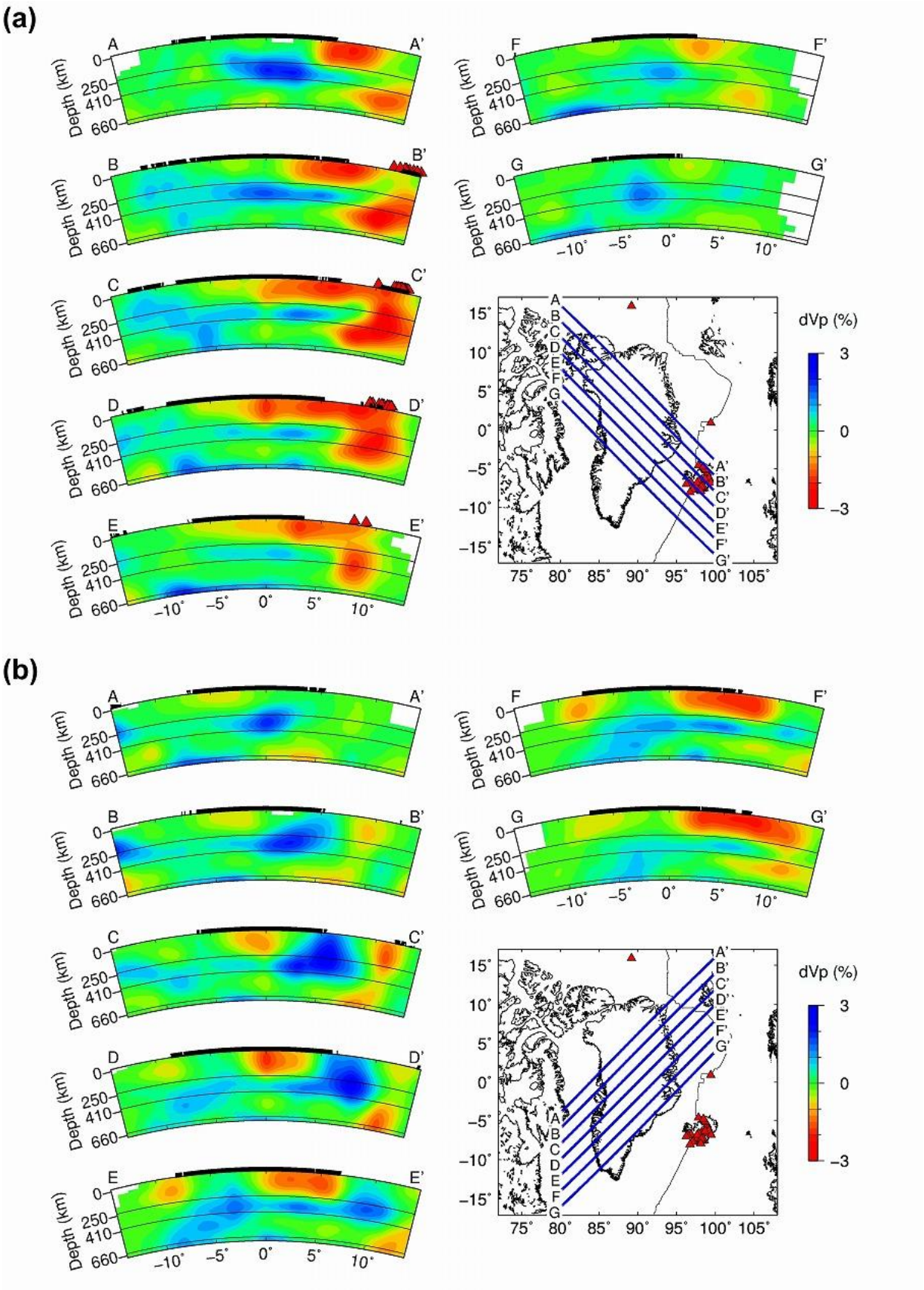
(a)
(b)
A
A'
B
B'
C
C'
D
D'
E
E'
F
F'
G
G'
Depth (km)
0
250
410
660
−10°
−5°
0°
5°
10°
15°
10°
5°
0°
−5°
−10°
−15°
75°
80°
85°
90°
95°
100°
105°
dVp (%)
3
0
−3

983

984 **Figure 8**. The same as Fig. 7 but along **(a)** seven profiles in the NW-SE direction and **(b)** seven
985 profiles in the NE-SW direction.
986

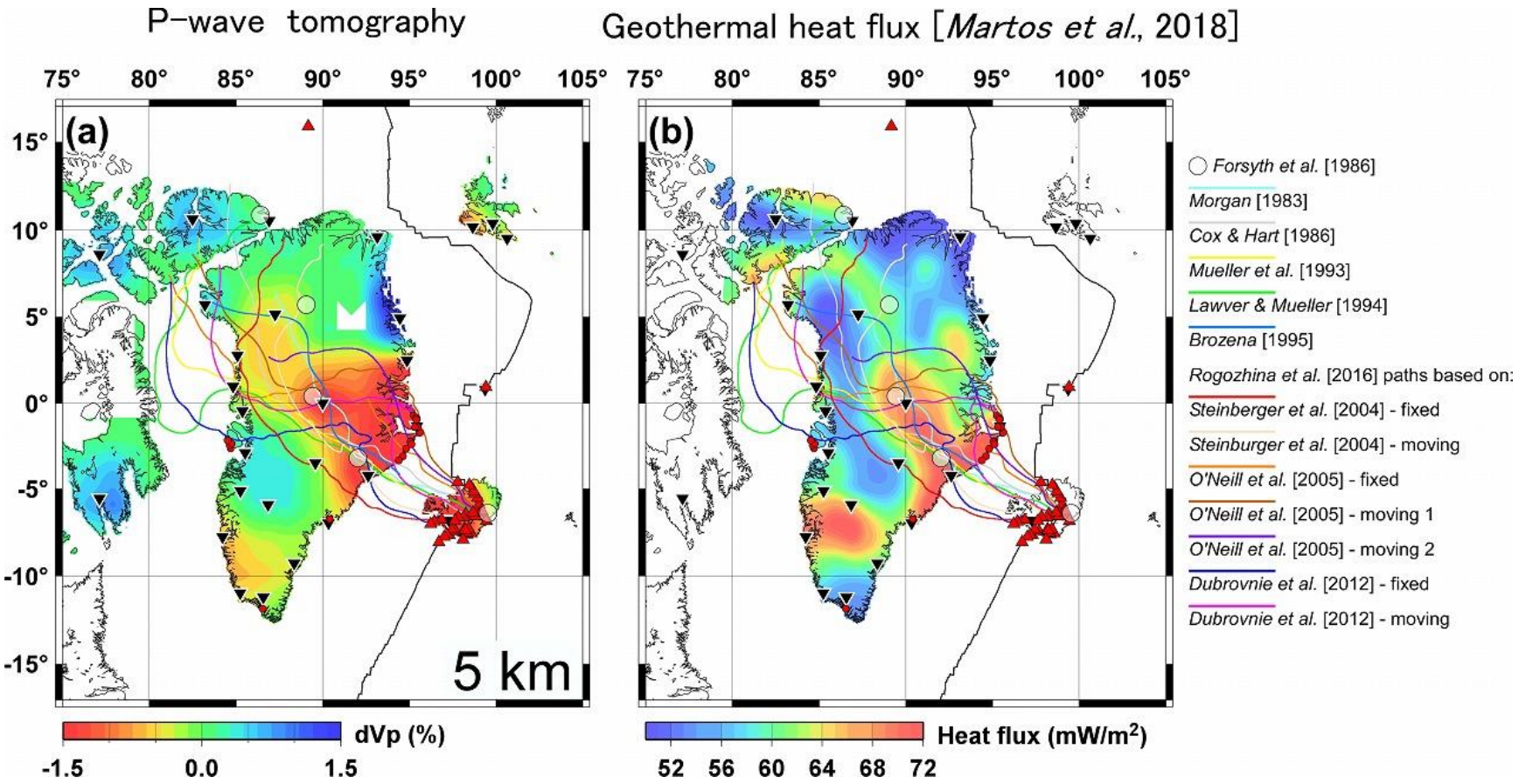

Figure 9. Comparison of the seismic velocity structure and crustal heat flow. **(a)** P-wave velocity tomography at 5 km depth obtained in this study. **(b)** Crustal heat flow from *Martos et al.* [2018]. The color lines denote the ancient tracks of the Iceland plume estimated by previous studies as shown on the right.

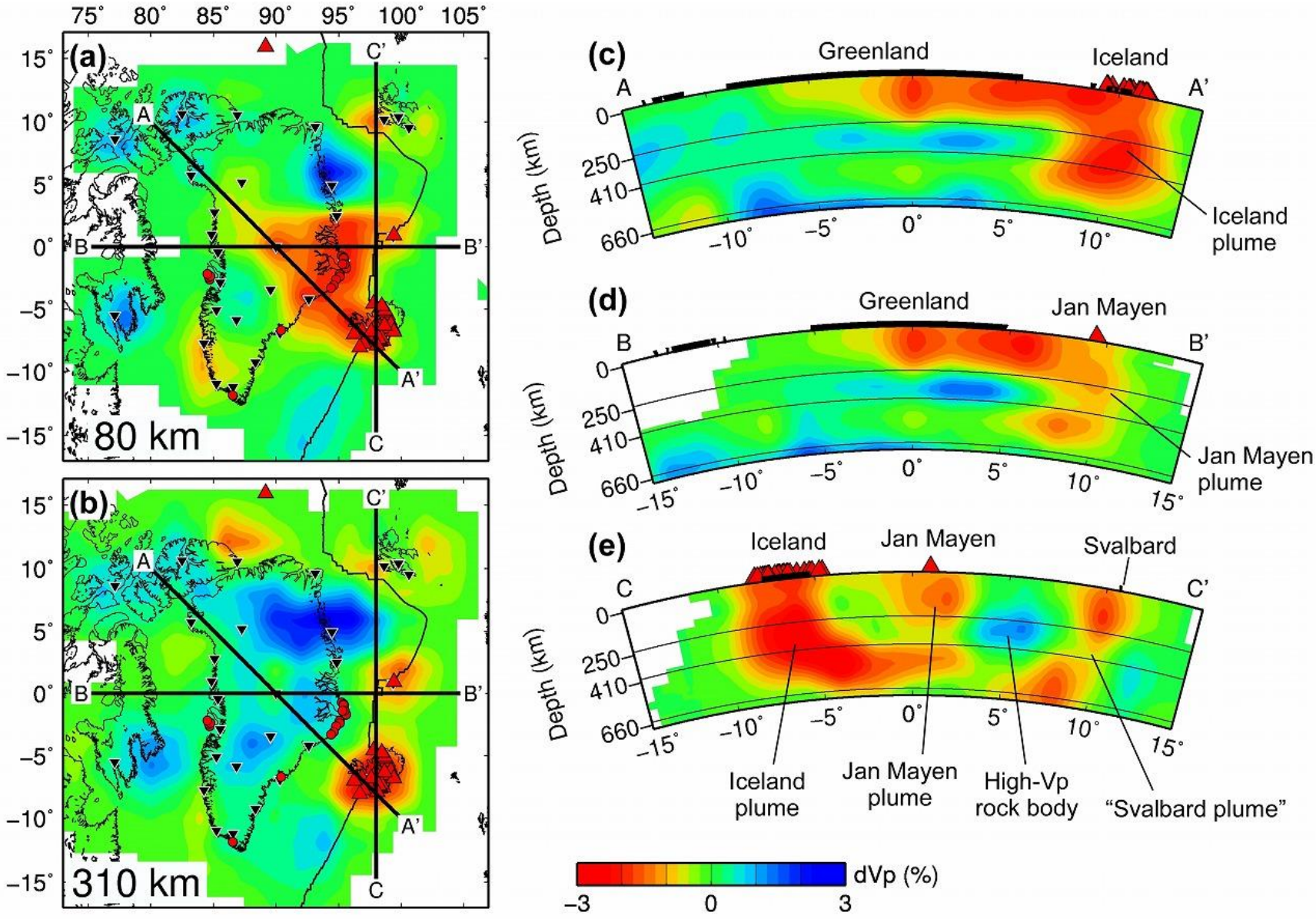
(a)
80 km
(b)
310 km
(c)
Greenland
Iceland
Iceland plume
(d)
Greenland
Jan Mayen
Jan Mayen plume
(e)
Iceland
Jan Mayen
Svalbard
Iceland plume
Jan Mayen plume
High-Vp rock body
"Svalbard plume"
Depth (km)
dVp (%)

993

Figure 10. Map views and vertical cross-sections showing main tectonic features in the study region. Map views at **(a)** 80 km and **(b)** 310 km depths. The symbols are the same as those in Fig. 6. **(c–e)** Vertical cross-sections along three profiles as shown in the map views. The symbols are the same as those in Figs. 7 and 8.

997 **Table 1**. Information on the seven tomographic inversions conducted by this study.

Name	Bottom depth of study region	Local events	Teleseismic events	Coordinate transformation	Crustal correction
Case 1	700 km	○	○	○	○
Case 2	700 km	○	−	○	−*
Case 3	700 km	−	○	○	○
Case 4	700 km	○	○	○	−
Case 5	700 km	○	○	−	○
Case 6	1500 km	○	○	○	○
Case 7	1500 km	○	○	○	−

998 * Local events do not require the crustal correction.